Spontaneous Chiral Ordering in Titanium Diselenide

by

Andrés M. Mier Valdivia

Submitted to the Department of Physics
in partial fulfillment of the requirements for the degree of

Bachelor of Science in Physics

at the

MASSACHUSETTS INSTITUTE OF TECHNOLOGY

June 2018

Signature redacted

Author .....
Department of Physics
May 11, 2018

Signature redacted

Certified by .....
Pablo D. Jarillo-Herrero
Associate Professor of Physics
Thesis Supervisor

Signature redacted

Accepted by .....
Scott A. Hughes
Interim Associate Department Head, Department of Physics

Spontaneous Chiral Ordering in Titanium Diselenide

by

Andrés M. Mier Valdivia

Submitted to the Department of Physics
on May 11, 2018, in partial fulfillment of the
requirements for the degree of
Bachelor of Science in Physics

Abstract

In this work, we studied the chiral charge density wave (CDW) phase in titanium diselenide ($TiSe_2$) with the circular photogalvanic effect (CPGE). Mechanically exfoliated bulk $TiSe_2$ flakes were obtained and implemented into nanoscale devices using standard fabrication techniques. Four samples' photocurrent response to a 120 meV laser was subsequently measured as a function of temperature and laser power. The onset of the CPGE at approximately 174 K confirms the emergence of chiral order below the regular CDW transition at 197 K. Furthermore, we were able to train the chirality of the system by cooling it while shining circularly polarized light. With this study, we have confirmed that $TiSe_2$ is a novel kind of material that spontaneously breaks inversion, all mirror, and roto-inversion symmetries and attains gyrotropic order, paving the way for future experimental work on similar condensed matter systems.

Thesis Supervisor: Pablo D. Jarillo-Herrero
Title: Associate Professor of Physics

Acknowledgments

I would like to thank Professor Pablo D. Jarillo-Herrero for the great opportunity to dive into the world of 2D materials. Thanks to his guidance, I have discovered my passion for the field and learned more than I could have ever expected. Furthermore, I would also like to thank Drs. Qiong Ma and Su-Yang Xu for their day-to-day help and patience. This work would not have been possible without them. I would also like to thank Yafang Yang for teaching me the foundations of nanofabrication during my initial time in the group. Furthermore, I am grateful to all members of the Jarillo-Herrero group for how welcoming and helpful they have been since I joined. Lastly, I would like to thank Wendi and my family for their constant support during my time at MIT.

Contents

List of Figures

Chapter 1

Introduction

In 2004, Drs. Andre Geim and Konstantin Novoselov successfully isolated graphene and measured its electrical properties [13]. The discovery opened the exciting new field of 2D physics. Since then, the number of known 2D materials has increased tremendously, and scientists are constantly unveiling novel behavior in new systems. Transition metal dichalcogenides (TMDs) are of particular interest due to the many phases they can assume despite their similar composition [1]. Some TMDs' band gap makes them a promising platform for innovations in semiconductor technology, while others have allowed physicists to study exotic states of matter such as superconductors and topological insulators. In this work, we focus on titanium diselenide ($TiSe_2$). Previous studies have suggested that, at low temperatures, $TiSe_2$ exhibits a chiral charge density wave (CDW) phase, a rare case of spontaneous chiral ordering [7] [9]. We seek to probe the chiral transition in the system by using the circular photogalvanic effect (CPGE), a technique sensitive to the symmetries of the system.

Chapter 2 presents a short overview of TMDs and their many properties. In Chapter 3, the basic physics of how a CDW forms and conducts electricity are explained. $TiSe_2$ and its CDW phase, along with the preliminary evidence for chiral ordering, are the subject of Chapter 4. Chapter 5 treats the CPGE and the information it can provide about any general system. The device fabrication is detailed in Chapter 6. In Chapter 7, we present and discuss our photocurrent data. Finally, Chapter 7 summarizes and concludes this work, in addition to suggesting future directions based

on our results.

Chapter 2

Overview of TMDs

2.1 Crystal Structure

A TMD monolayer consists of transition metal atoms sandwiched between two layers of chalcogen atoms (S, Se, or Te) as shown in Figure 2-1a. The bulk crystal consists of successive monolayers stacked on each other, bound together by the van der Waals force. The weak interlayer coupling means TMDs can be mechanically exfoliated with tape down to the monolayer limit. The sticky tape technique has proven to be a reliable method for obtaining high-quality samples that can be implemented into nanoscale heterostructures [14]. The two most common crystallographic orientations for TMDs are the trigonal prismatic (2H) phase and octahedral (1T) structures [1]. Another important phase is the orthorhombic ($1T_d$) structure, currently only observed in tungsten ditelluride (WTe_2).

2.2 Electronic Structure

The electronic properties of TMDs depend sensitively on the material thickness. Often, ultrathin flakes have a completely different electronic structure than the bulk. The difference often arises from symmetries broken due to reduced dimensionality, and as a consequence of confining the electrons to an increasingly 2D volume. For example, the semiconductor molybdenum disulfide (MoS_2) has a direct band gap in its

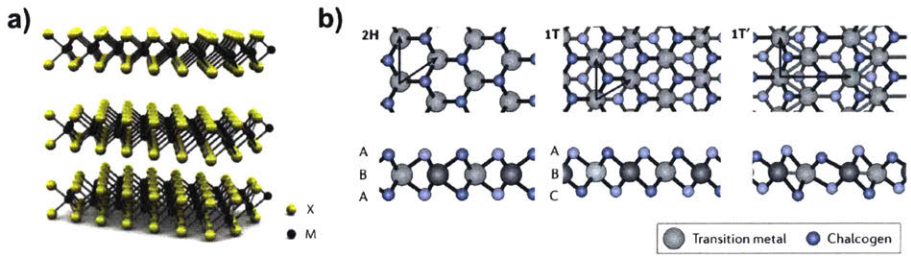

Figure 2-1: **(a)** TMDs consist of transition metal M atoms sandwiched between chalcogen X atoms. **(b)** The most common crystallographic phases observed in TMDs. Figures adapted from [1] [2].

monolayer form, while thicker flakes have an indirect gap [15] [16]. The effect can be explained by the hybridization of the sulfur p-orbitals with the molybdenum d-states. The thickness-dependent behavior can also be opposite for different materials. In niobium diselenide ($NbSe_2$), superconductivity weakens with decreasing layer thickness [17], while in tantalum disulfide (TaS_2) superconductivity is enhanced [18] [19]. As already alluded to above, TMDs exhibit a wide variety of phases despite their similar composition. Superconductors, CDW conductors, topological insulators, and other novel states are all represented in this family of van der Waals crystals. Figure 2-2 summarizes the many phases so far identified, with recent results even suggesting that different phases can be achieved by tuning the electron density with gate voltages [20].

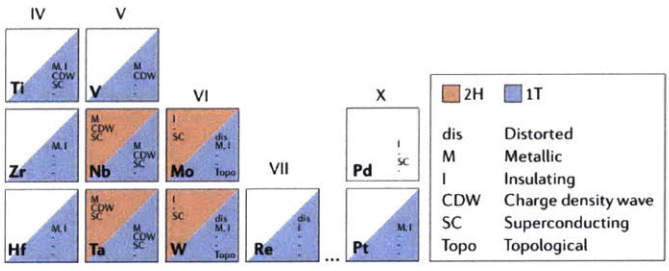

Figure 2-2: A table summarizing TMD crystal structure and observed electronic phases based on the transition metal. Figure adapted from [1].

2.3 Optical Properties

In gapped TMDs, photons can excite valence band electrons into the conduction band. As excess carriers recombine, photons are emitted with an energy corresponding to the band gap [21]. Therefore, photoluminescence (PL) is a powerful tool for studying TMDs. As an example, thanks to the direct band gap in monolayer MoS_2, the PL quantum efficiency is 104 times stronger than in the bulk [16]. Additionally, when electrons are excited into the conduction band, they leave behind a hole in the valence band. Due to the Coulomb interaction, the electron and hole feel an electrostatic attraction and can form a quasiparticle state called an exciton [21]. Trions, an exciton plus an extra hole or electron, can also form. Exciton and trion recombination leads to photoemission that can be captured in PL spectra. Currently, excitons in 2D systems are an active area of research. Since the quasiparticles are bosons, theorists have postulated that they could form a Bose-Einstein condensate [22]. However, this has yet to be realized, in part due to the short lifetime of an electron-hole pair. Efforts are underway to achieve excitonic condensation in bilayer TMD systems such as $MoSe_2$-WSe_2 heterostructures [23].

Chapter 3

Charge Density Wave Physics

Charge density waves (CDWs) were first predicted in 1929 by Rudolph Peierls when he noted that a 1D atomic lattice was thermodynamically unstable at $T = 0$ K [24]. Since the 1970s, there has been an explosion in the discovery of low-dimensional materials that have been found to host CDWs, such as $NbSe_3$, $K_{0.3}MoO_3$ and KCP [4] [3], in addition to TMDs such as TaS_2 and $TiSe_2$. This chapter is dedicated to explaining the basic physics behind CDW formation and the resulting electrical properties.

3.1 The Peierls Transition

Consider a one-dimensional atomic chain with lattice constant a and corresponding constant electronic density $\rho(r) = \rho_0$, such as that shown in Figure 3-1a. In k-space, the Brillouin zone has edges at $\pm\pi/a$, and only the electronic energy levels up until the Fermi level E_F are occupied.

If electron-phonon interactions are introduced, the underlying lattice is no longer stable. A periodic real-space lattice distortion of the form $\delta r = \delta r_0 \cos\left(\frac{2\pi}{\lambda} r + \phi\right)$ for $\lambda = 2a$ becomes favorable and leads to the opening of a gap 2Δ at the Fermi wavevector $k_F = \pi/2a$ as shown in Figure 3-1b. All the electronic states collapse to the lower band, and the overall energy is lowered. The new electronic density is given by $\rho_r = \rho_0 + \rho_1 \cos(2k_F r + \phi)$, which leads to periodic charge ordering; in other words, a charge density wave. The emergence of a superlattice further causes the

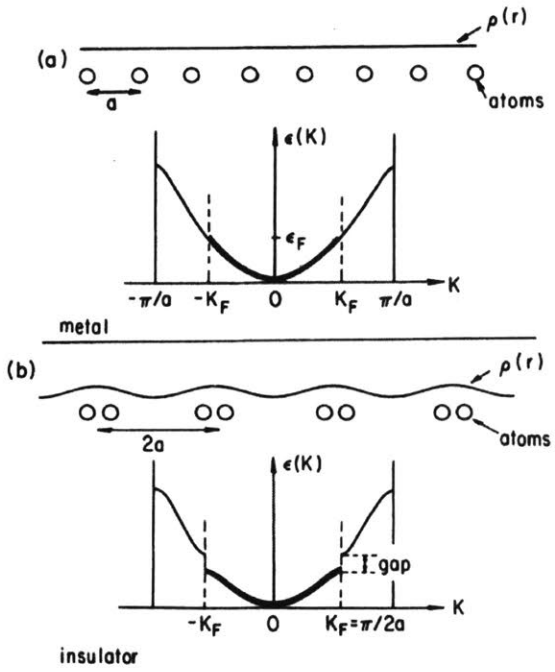

Figure 3-1: The Peierls transition in a 1D metal. **(a)** A 1D atomic lattice with constant a. $\rho(r)$ is the electron density; in this case it is constant. The Brillouin zone is shown below it, and only the energy levels up the Fermi level E_F are filled (ϵ_F in the figure). **(b)** Because the metal is unstable at $T = 0$ K, a gap opens at the Fermi level and a superlattice with spacing $2a$ forms. The Brillouin zone reduces to half of its original size and leads to band folding at $\pm k_F$. Figures adapted from [3].

bands to fold at k_F, so the CDW-state Brillouin zone is reduced in half. In reality, the ratio λ/a is not necessarily a rational number and will depend on the material's Fermi energy.

At finite temperatures, thermal excitations entail a gap reduction, until at T_{CDW} the system undergoes a second-order transition into a normal state. The mean-field order parameter $\psi = \Delta e^{i\phi}$ characterizes the phase transition. The variable Δ measures the size of the gap and is proportional to the atomic displacement amplitude δr_0. The phase ϕ sets the relative shift between the charge modulation and the normal-state lattice. In real materials, CDWs tend to form in systems composed of weakly coupled chains, such that electron motion is easier along the chains than in the perpendicular directions. This feature lends the system a quasi-1D character that allows the formation of charge order at low temperatures.

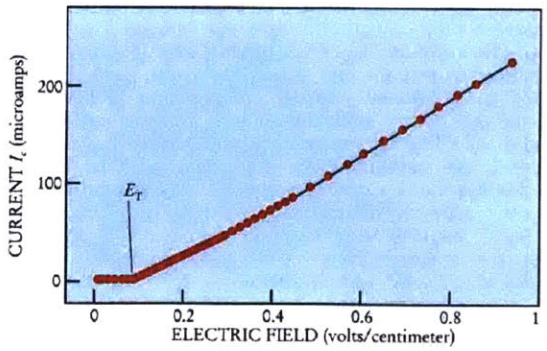

Figure 3-2: Typical current versus electric field behavior for CDW conductors. There is no conductance below E_T, after which charge order slides relative to the lattice and generates a current. In this particular graph, the data is for $NbSe_3$ at 120 K. Figure adapted from [4].

3.2 Electrical Properties of CDWs

Importantly, the emergence of a gap means that the transport properties of the system change. In theory, the phase ϕ can take on any value without changing the ground state energy, so all configurations of the charge order relative to the lattice are equal, which would imply that dissipationless currents can flow in the CDW phase, and so the material should also be a superconductor. However, this is not the case due to the presence of defects and impurities. When λ/a is commensurate, the CDW will align with the underlying lattice and the application of an external field will translate the CDW relative to its preferred orientation, leading to energy oscillations with period λ. In the incommensurate case, the presence of impurity and disorder creates local minima, and the CDW becomes "pinned" into a particular configuration. Thus, it is necessary to apply a sufficiently large threshold electric field E_T before the material becomes conducting, as shown in Figure 3-2.

Once E_T is overcome, the material conducts thanks to the CDW sliding, shown in Figure 3-3. As the atoms oscillate back and forth, the charge potential slides relative to the underlying lattice. The conduction electrons can ride the CDW and generate an electrical response.

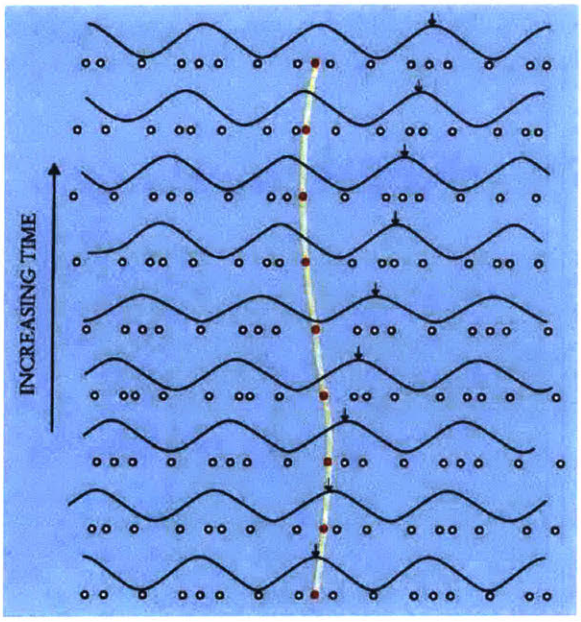

Figure 3-3: When E_T is overcome, the CDW slides. The lattice atoms oscillate, as traced by the yellow path that follows the position of the red particle. The effect allows the potential to move towards the right, illustrated by the traveling black arrow. Figure adapted from [4].

Chapter 4

The Charge Density Wave in 1T-$TiSe_2$

In this chapter, we will discuss 1T-$TiSe_2$ ($TiSe_2$ hereinafter), our material of interest. Its crystal structure and Brillouin zone are shown in Figure 6-4. $TiSe_2$ exhibits a CDW phase below T_{CDW}. Previous experimental work has further suggested that below another transition temperature T_{chiral}, the system spontaneously attains chiral order. Here, we highlight some of the previous work done on the regular CDW phase in $TiSe_2$, and motivate our experiment to probe the chiral CDW structure with the CPGE.

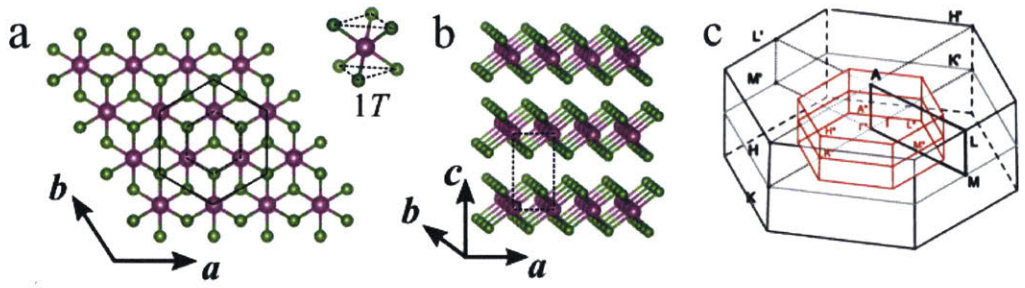

Figure 4-1: Crystal structure of 1T-$TiSe_2$. The purple atoms are Ti, and the green are Se. **(a)** Top view of a monolayer. **(b)** Crystal sideview. **(c)** Brillouin zone.

4.1 The CDW Transition

Angle-resolved photoemission spectroscopy (ARPES) on monolayer $TiSe_2$ reveals a commensurate $2 \times 2 \times 2$ CDW transition at $T_{CDW} = 232 \pm 5$ K [5]. Figure 4-2b shows the band structure obtained from ARPES at room temperature and at 10 K, well below the CDW transition. At room temperature, there are two convex bands near

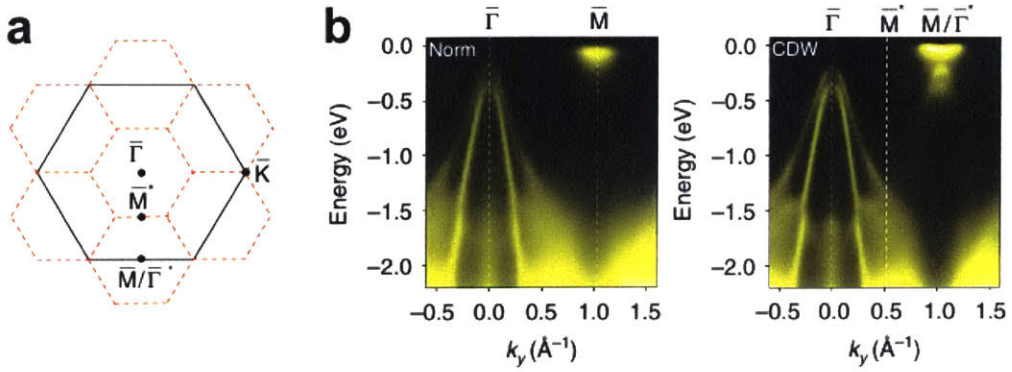

Figure 4-2: ARPES data for monolayer $TiSe_2$. **(a)** In solid black: the normal-state Brillouin zone of $TiSe_2$. In dashed red: the reduced Brillouin zone in the CDW phase. **(b)** On the left: the normal state ARPES data taken at room temperature. On the right: the CDW state ARPES data taken at 10 K. Note the appearance of a new band at $\bar{M}/\bar{\Gamma}$ due to band folding. Figures adapted from [5].

the Fermi level at the $\bar{\Gamma}$ point, arising from the Se $4p$ states. Additionally, there is a top band at the Brillouin zone boundary $\bar{M}$ originating from the Ti $3d$ orbitals. Both features give rise to an experimentally measured indirect band gap of 98 meV.

At 10 K, the monolayer is in the CDW state, which leads to a superlattice structure with double the periodicity of the natural crystal lattice. In turn, the Brillouin zone shrinks to half the original size and leads to band folding, as shown in Figure 4-2a. The new k-space zone boundary is demarcated by $\bar{M}^*$, and $\bar{M}$ becomes the central $\bar{M}/\bar{\Gamma}^*$ point of an adjacent zone. The effect can be seen in the low temperature band structure data from Figure 4-2b. At $\bar{\Gamma}$, the Se $4p$ bands retain their shape, although they are pushed down in energy. Thanks to band folding, a duplicate of the convex bands appears at $\bar{M}/\bar{\Gamma}^*$. The new bands have a weaker intensity since the CDW distortion is inherently weak. The band gap at 10 K is measured to be 153 meV,

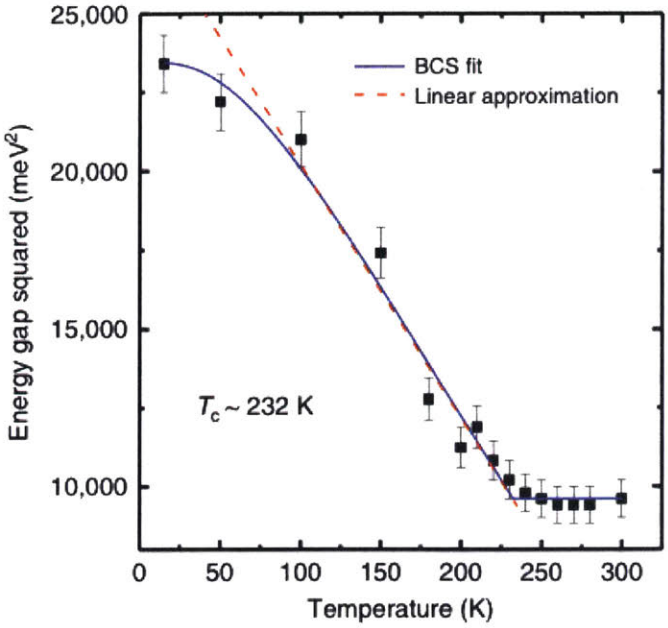

Figure 4-3: Temperature dependence of the band gap as measured from the ARPES spectra for monolayer $TiSe_2$. The solid blue line is a BCS-type fit. The dashed red line is a linear approximation. The BCS-type fit gives $T_{CDW} = 232 \pm 5$ K. Figure adapted from [5].

larger than in the normal state value of 98 meV. A full temperature dependence of the gap is shown in Figure 4-3. The gap remains constant above T_{CDW}, but widens below it. The results are well described by mean-field theory.

The thickness dependence of the band gap and T_{CDW} is shown in Figure 4-4 [6]. Increased dimensionality rapidly suppresses charge ordering, and T_{CDW} already converges to the bulk value of 205 K in a trilayer. This suggests that the CDWs in adjacent layers interact strongly, the overall effect leading to a weakening of the charge ordered phase. The bilayer data is an interesting case that highlights the transition from a 3D crystal to a 2D system. It exhibits two transitions with $T_{CDW,1} = 236 \pm 5$ K and $T_{c,2} = 195 \pm 3$ K. The interpretation is that at $T_{CDW,1}$, which is close to the monolayer T_{CDW}, the individual layers develop noninteracting CDWs independently of each other. Subsequently, at $T_{CDW,2}$, similar to the bulk T_{CDW}, the layers begin to interact and the CDWs lock into an antiphase arrangement. Surprisingly, even the bilayer exhibits bulk-like behavior.

The formation of the CDW phase in $TiSe_2$ is still poorly understood and hotly

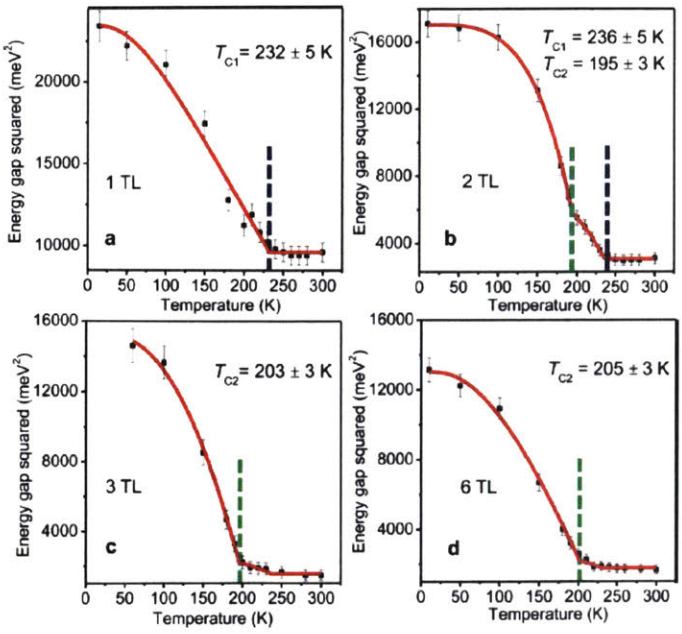

Figure 4-4: Thickness dependence of T_{CDW} for $TiSe_2$. The individual plots show the band gap evolution from ARPES data versus temperature. The transition temperatures were computed with a BCS-type fit. **(a)** Monolayer data with $T_{CDW} = 232 \pm 5$ K. **(b)** Bilayer data. Note that there are two transition temperatures at $T_{CDW,1} = 236 \pm 5$ K and $T_{CDW,2} = 195 \pm 3$ K. **(c)** Trilayer data with $T_{CDW} = 203 \pm 3$ K. **(d)** 6-layer data with $T_{CDW} = 205 \pm 3$ K. Figure adapted from [6].

debated [10]. There are currently three main theoretical proposals, all of which are supported by experimental results [25] [26] [27]. One model argues that charge order arises thanks to strong electron-phonon coupling in what is known as the Jahn-Teller (JT) effect. In this scenario, the in-plane Ti-Se bonds shorten, leading to an overall reduction of the local bond energy and a kinetic energy gain. This manifests itself as a lowering of both the top and bottom bands, which is observed to become amplified below T_{CDW}, suggesting the JT effect is the driving force towards charge order. A second perspective is that $TiSe_2$ becomes an excitonic insulator (EI) primarily due to electron-electron interactions. Below T_{CDW}, it becomes favorable for an electron to hop from an Se pocket to a Ti atom, leaving behind a hole. Thanks to poor Coulomb screening, the electron and hole feel a mutual attraction and form an exciton. The electrostatic attraction will cause a lattice distortion, leading to a CDW. The final proposed mechanism is a combination of both the JT effect and EI formation. A lat-

tice distortion from the JT mechanism will lead to a shortening of the bond length, facilitating the hopping of an electron and thus the formation of an exciton. Likewise, the electron-hole attraction will shorten the Ti-Se length and amplify the JT effect. To first order in perturbation theory, electrons can only hop between neighboring in-plane Ti-Se atoms, forming a series of 1D chains that lead to a CDW. Theoretical work has found that just the JT or EI effects are insufficient to quantitatively describe experimental results, which lends support to the cooperation between both mechanisms as the driving force for charge order in the material.

4.2 Experimental Evidence for a Chiral CDW

From the thickness dependence of the CDW transition, we can already see that the interlayer CDW interaction is nontrivial. In a scanning tunneling microscopy (STM) experiment, Ishioka *et al.* observed evidence for a chiral CDW structure in bulk $TiSe_2$ [7]. Figure 4-5a shows their STM data for a sample at 84 K. The bright spots

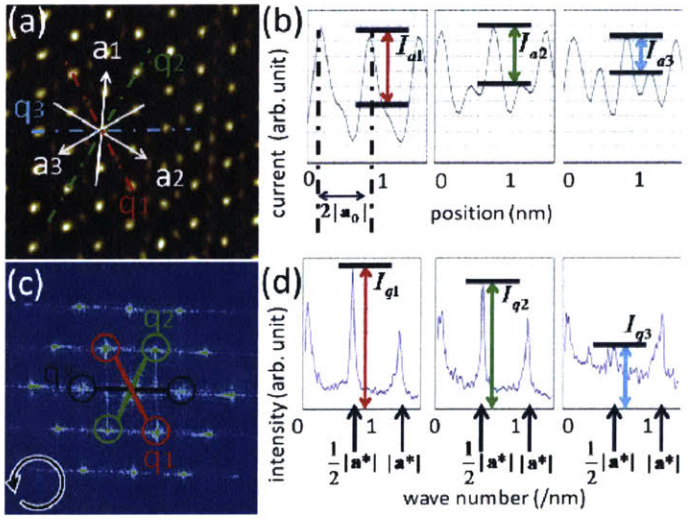

Figure 4-5: STM data for a bulk TiSe2 sample at 84 K. **(a)** Real space STM data where the CDW is apparent. The $\mathbf{a}_i$ vectors designate the three crystallographic directions, and the $\mathbf{q}_i$ indicate the directions of charge modulation. **(b)** Line intensities along the three distinct $\mathbf{q}_i$ in real space. **(c)** Fourier transform of (a). Note how the intensity increases CCW from $\mathbf{q}_3$ to $\mathbf{q}_1$. **(d)** Line intensities along the different $\mathbf{q}_i$ in Fourier space. Figure adapted from [7].

correspond to regions of high tunneling current; these are the positions of the Se atoms in the lattice. The spots are arranged in a triangular configuration with constant a_0, as expected for the material. However, note the varying intensities of the spots. Upon closer inspection, it is possible to define three vectors $\mathbf{q}_i$ along which the intensity varies with a period of $2a_0$. This modulation is due to the CDW superlattice (at 84 K, the sample is well below $T_{CDW} = 205$ K). What is surprising is the presence of three distinct directions with different peak intensities, evident in Figure 4-5b. The variation becomes more apparent in the Fourier transform of the data, shown in Figure 4-5c. The intensity increases counterclockwise (CCW) starting from $\mathbf{q}_3$ and rotating towards $\mathbf{q}_1$, as presented in Figure 4-5d.

STM data from a second sample at 6.3 K is shown in Figure 4-6. The sample

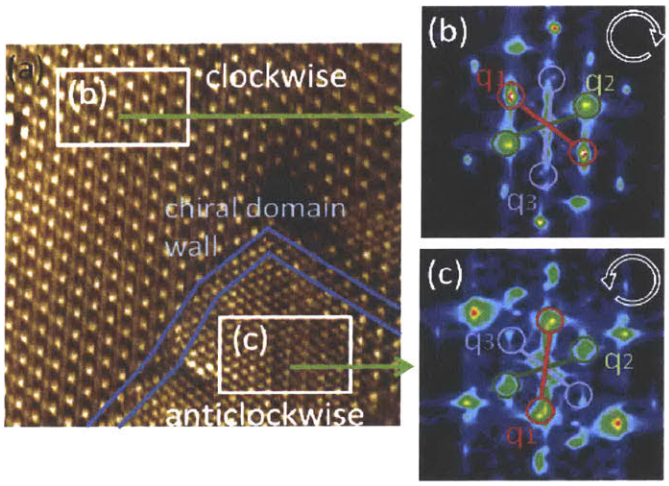

Figure 4-6: **(a)** A real space 12 nm × 12 nm STM image of a sample at 6.3 K. The blue lines denote the domain wall between the CW and CCW chiral phases. **(b)** and **(c)**: the Fourier transform of the data enclosed by the squares in the CW and CCW regions, respectively. Figure adapted from [7].

exhibits a clockwise (CW) (Figure 4-6b) and a CCW phase (Figure 4-6c) coexisting in the same lattice, separated by a domain wall. The surprising result led Ishioka *et al.* to postulate that the CDW in $TiSe_2$ points along a different direction in each successive layer. The direction of $\mathbf{q}_i$ rotates either CW or CCW in successive layers, forming a chiral structure whose handedness is defined by $h_{CDW} = \mathbf{q}_1 \cdot (\mathbf{q}_2 \times \mathbf{q}_3)$. They argue that in their data, they can resolve the top three layers and that the varying

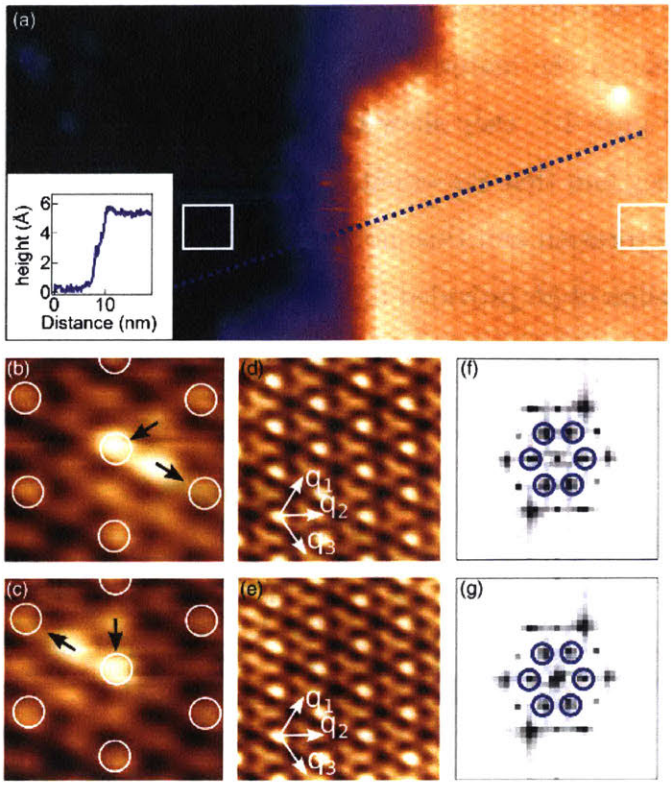

Figure 4-7: Data take n at 4.6 K. **(a)** A 20 nm × 10 nm STM image of a step between two successive $TiSe_2$ layers. The inset shows the height difference between the layers of 6 Å, corresponding to the size of one Se-Ti-Se sandwich. **(b), (c)** An enlargement of the white squares in (a) corresponding to defects in the bottom and top layers, respectively. The circles highlight the charge maxima, and the arrows indicate the direction of atomic displacements. **(d), (e)** 2.8 nm × 2.8 nm STM images of the bottom and top layers, respectively, showing that the orientation of the $\mathbf{q}_i$ is the same for both.**(f), (g)** Fast FT of (d), (e) where the blue circles highlight extra features owing to the CDW. Figure adapted from [8]

intensity along each $\mathbf{q}_i$ is because tunneling from the inner layers is exponentially suppressed given that the probe is further away. This point is one reason why the experiment is not conclusive in identifying chiral ordering: STM cannot probe long range order in the bulk. Additionally, all the measurements were carried out well below T_{CDW}, so the paper provides no information about a phase transition from a normal CDW to a chiral ordered phase.

Another STM experiment by Hildebrand *et al.* further disputed the claims by Ishioka *et al.* [8]. They showed that STM is actually only sensitive to the topmost Se

layer in a Se-Ti-Se sandwich, so the technique cannot provide any information about the long range order in the material. In fact, their results indicate that the CDW is non-chiral. In Figure 4-7, they show the STM data for a step between two $TiSe_2$ layers at 4.6 K. They find that the orientation of the $\mathbf{q}_i$ is the same for both, showing there is no relative rotation and thus no handedness.

However, Castellan *et al.* provided further evidence for the chiral phase [9]. Using x-ray diffraction, which is sensitive to the lattice periodicity, they probed the phase transition. Their data is shown in Figure 4-8a. As a function of temperature, they

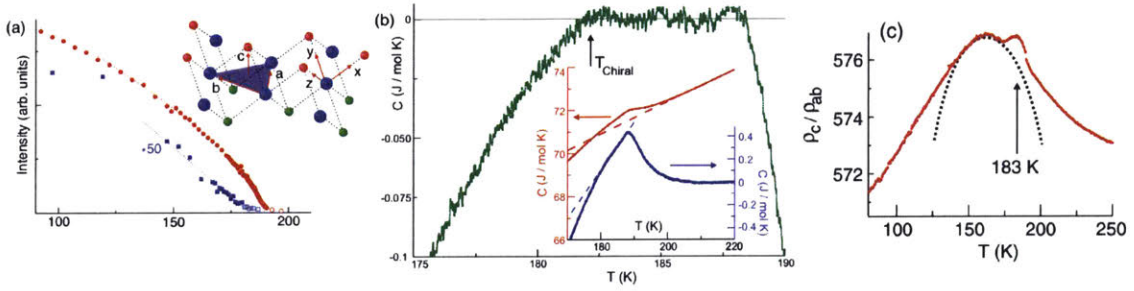

Figure 4-8: Evidence for a phase transition at 183 K. **(a)** X-ray diffraction peak intensities as a function of temperature. The red points follow a peak sensitive to the formation of the regular CDW superlattice. The blue data is for another peak that turns on around 183 K. **(b)** Specific heat as a function of temperature. **(c)** Resistivity anisotropy as a function of temperature. Figures adapted from [9].

tracked the intensity of the $[\frac{3}{2}, \frac{3}{2}, \frac{1}{2}]$ reflection, sensitive to the formation of a superlattice corresponding to the onset of a CDW. The peak turns on at $T_{CDW} = 190$ K (slightly below the $T_{CDW} = 205$ K due to stoichiometric imperfections in the crystal growth). However they also tracked a peak from the $[\frac{5}{2}, 1, 0]$ reflection. Although not forbidden in a non-chiral ordered phase, the authors observed that the peak suddenly turns on at $T_c = 183$ K. This is indicative of a second phase transition, which the researchers take to be the onset of helical CDW ordering.

Castellan *et al.* further supported their claim with specific heat measurements, shown in Figure 4-8b. The specific heat peaks around T_{CDW}, briefly saturating before suddenly decreasing at T_c. Additionally, Figure 4-8c shows the resistivity anisotropy ρ_c/ρ_{ab}, a quantity that measures the difference in electron transport in the out-of-plane versus in-plane directions. They also identified a peak in the data around T_c.

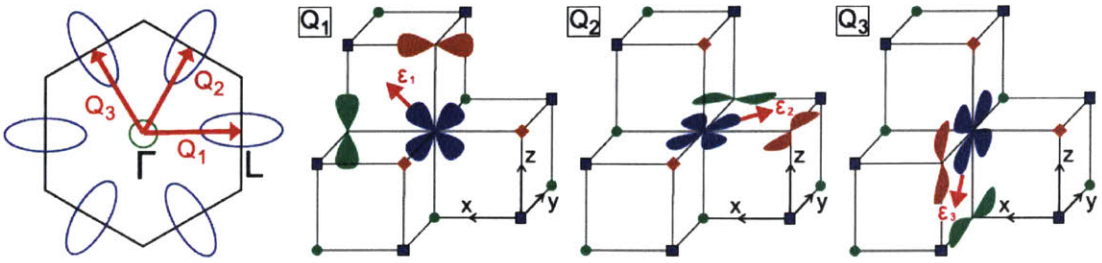

Figure 4-9: Illustration of the Brillouin zone and the three inequivalent directions for orbital and charge ordering. Figure adapted from [10].

The three different kinds of measurements by Castellan *et al.* are sufficient to show that there are two distinct transitions at T_{CDW} and T_c. Although the transition at T_{CDW} can be safely attributed to the onset of CDW order given the x-ray diffraction data, T_c cannot be confidently accounted for by chiral ordering. None of the measurements performed in the paper were sensitive to chirality, so although there is clearly a phase transition at 183 K, it is not necessarily due to the emergence of chiral charge ordering.

4.3 A Model for a Chiral CDW

Chirality is not uncommon in systems where the order parameter is a vectorial quantity, such as in magnetic materials [10]. However, electron density is a scalar quantity so it is not immediately clear how chiral order can form. The transition can be understood as the formation of both charge and orbital order. Although the mechanism behind the formation of the normal CDW phase is still poorly understood, the transition from non-chiral to chiral order can be effectively described with Ginzburg-Landau theory [10].

Figure 4-9 shows the Brillouin zone for $TiSe_2$. In the CDW phase, electron density is shifted from the central $\bar{\Gamma}$ pocket to one of the edge Ti pockets. Because there are three independent Ti pockets, there are three distinct directions $\mathbf{Q}_i$ along which orbital and charge order can polarize. Thus, the total lattice distortion from the

CDW is a superposition of the atomic displacements along the three inequivalent directions. We also need to consider relative phase shifts arising from Coulomb and phonon interactions. Therefore, the total atomic distortion $\delta\mathbf{x}$ will be given by

$$\delta\mathbf{x} \propto \sum_{i}^{3} \epsilon_i \cos(\mathbf{Q}_i \cdot \mathbf{x} + \phi_i)$$

Now, consider the charge density modulation $\alpha = \mathbb{R}\{\sum_j^3 \psi_j\}$ for order parameters $\psi_j = \psi_0 e^{i\mathbf{Q}_j \cdot \mathbf{x} + \phi_j}$. The associated Landau free energy is

$$F = \int \mathrm{d}\mathbf{x}_i \; a(x)\alpha^2 + b(x)\alpha^3 + c(x)\alpha^4 + d(x)(|\psi_1\psi_2|^2 + |\psi_2\psi_3|^2 + |\psi_3\psi_1|^2)$$

for some coefficients $a(x)$, $b(x)$, $c(x)$, and $d(x)$ that encode the lattice periodicity and unit cell structure. To account for this, we choose their form as follows

$$a(x) = a_0 + a_1 \sum_j e^{i\mathbf{G}_j \cdot \mathbf{x}} + a_1\gamma \sum_{j,k} e^{i\mathbf{G}_j \cdot (\mathbf{x} + \mathbf{R}_k)} + \ldots$$

where $\mathbf{G}_j$ are the reciprocal lattice vectors, $\mathbf{R}_k$ measures the distance between neighboring Ti and Se sites, and γ depends on the electron-phonon coupling.

The free energy becomes

$$F = \frac{3}{2}a_0\psi_0^2 + \frac{1}{2}a_1\psi_0^2(1-\gamma)\sum_j \cos(2\phi_j) + \frac{3}{8}(15c_0+8d_0)\psi_0^4 + \frac{3}{4}c_2\psi_0^4 \sum_j \cos(2\phi_j - 2\phi_{j+1}) \tag{4.1}$$

We obtain two ground states by minimizing (4.1) with respect to ϕ_j. The first corresponds to a regular non-chiral phase with $\phi_1 = \phi_2 = \phi_3 = \frac{\pi}{2}$. The second solution has $\phi_1 = \frac{\pi}{2}$, $\phi_2 = -\phi_3$, and $\phi_3 = \pm 1/2 \cos^{-1}[(3c_2\phi_0^2 - 2a_1(1-\gamma))/(6c_2\phi_0^2)]$. This is the chiral phase in which there is a relative phase between the $\mathbf{Q}_i$. The free energies associated with both configurations are

$$F_{non-chiral} = \frac{3}{2}a_0\psi_0^2 + \frac{3}{8}(15c_0 + 8d_0)\psi_0^4 - \frac{3}{2}a_1\psi_0^2(1-\gamma) + \frac{9}{4}c_2\psi_0^4$$

$$F_{chiral} = \frac{3}{2}a_0\psi_0^2 + \frac{3}{8}(15c_0 + 8d_0)\psi_0^4 - \frac{a_1^2(1-\gamma)^2}{6c_2} - \frac{9}{8}c_2\psi_0^4$$

Because the chiral phase requires a nonzero ψ_0, the system must first transition into the non-chiral phase before acquiring chiral order at a lower temperature T_{chiral}. Assuming $a_0 = \bar{a}(T - T_{CDW}) + a_1(1 - \gamma)$ encodes all the temperature dependence of the system, and minimizing F with respect to ψ_0, the chiral state becomes more energetically favorable when $\psi_0^2 = \frac{2a_1(1-\gamma)}{9c_2}$. Therefore, the chiral transition temperature will be

$$T_{chiral} = T_{CDW} - \frac{a_1(1-\gamma)(15c_0 + 8d_0 + 6c_2)}{9\bar{a}c_2}$$

The second derivative of the free energy $\frac{d^2F}{dT^2}$ is discontinuous across T_{chiral}, so the transition from normal charge order to a chiral state is of the second order. The chiral transition temperature of 183 K observed by Castellan *et al.* is in agreement with this model.

4.4 The CPGE as a Probe for Chirality

The two experiments probing the chiral CDW in $TiSe_2$ were insufficient to prove its existence. The STM experiment by Ishioka *et al.* was only sensitive to surface features, did not observe a phase transition, and was contradicted by another STM study. The experiments by Castellan *et al.* provided evidence for a phase transition in addition to the well-studied CDW one, but they failed to probe the resulting state's chirality. We propose to show the emergence of a chiral phase by using the CPGE. Because the CPGE is sensitive to broken symmetries, it should be able to detect the lack of inversion, all mirror, and roto-inversion symmetries that is characteristic of chiral systems. Additionally, it can be easily performed at various temperatures, which would allow us to probe the transition and identify T_{chiral}. In the next chapter, we describe in more detail the CPGE and its capabilities.

4.5 Degradation

$TiSe_2$ has been shown to oxidize under ambient conditions, manifesting as a suppression of the CDW [11]. Sun *et al.* found that as-exfoliated flakes between 5-8 nm thick

were fully degraded by the time they measured them as they did not show any CDW transition. In flakes of thicknesses between 8-20 nm, they found that the resistivity increased in time until the samples became fully insulating after about 15 days, as shown in Figure 4-10 for an 11 nm flake. Thicker flakes were much more robust and their CDW properties persisted for months.

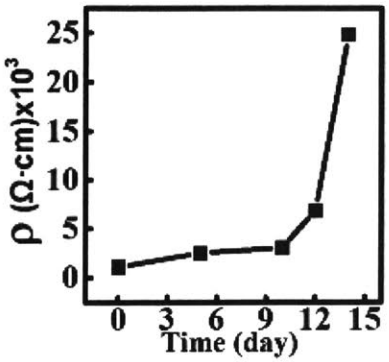

Figure 4-10: Room temperature resistivity as a function of time (in days) for an 11 nm $TiSe_2$ thick flake. The resistivity shows a clear increase around 12 days, and a large spike after 15 days. Figure adapted from [11].

Figure 4-11a,b shows the transmission electron microscopy (TEM) image of a $TiSe_2$ flake. After one month, the effect of the degradation is apparent given the visible change in the contrast of the TEM images. This is further suggested by Figure 4-11c,d, which shows the atomically resolved high-angle annular dark-field scanning TEM (HAADF-STEM) images for the same flake. Right after exfoliation, the TEM can clearly capture the individual Ti and Se atoms present in the lattice. After a month, however, the pattern is no longer visible and the image resembles the white noise pattern, indicating the previous order was lost and that the structure has become amorphous.

The suggested mechanism is an oxidation-selenium intercalation. The O_2 in the atmosphere reacts with the surface layers to form TiO_xSe_{2-x}. Eventually, the unstable Ti-O-Se bonds break naturally, and the Ti atoms become TiO_2 as the Se atoms are pushed in between the layers. The accumulation of Se widens the gap between layers, allowing O_2 to creep in and further oxidize the sample. The process continues until the $TiSe_2$ has fully degraded into amorphous TiO_2 and pure Se. Thus, for bulk flakes,

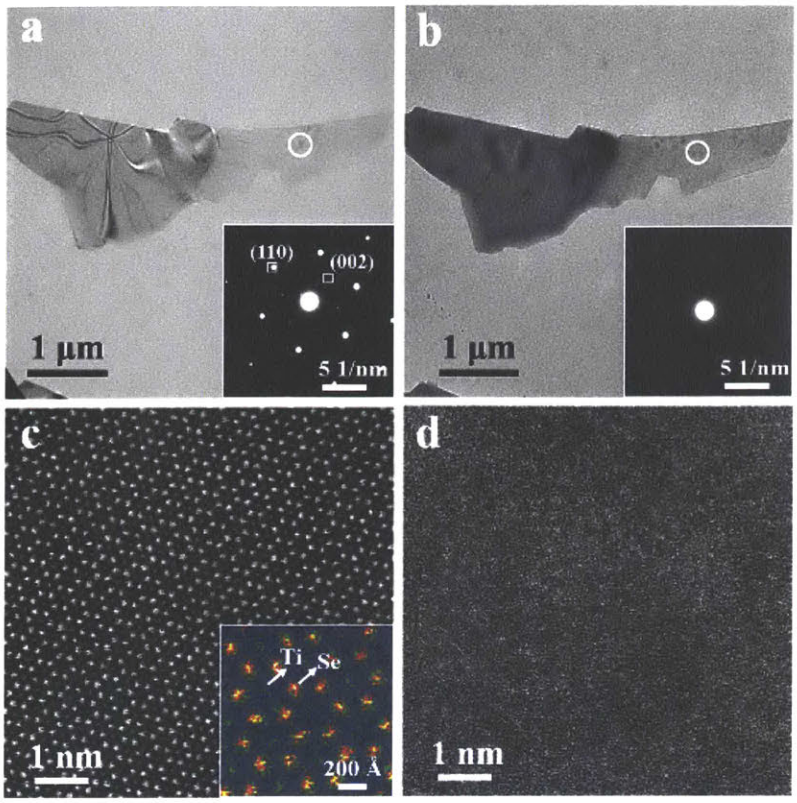

Figure 4-11: Degradation in $TiSe_2$. **(a),(b)** TEM images of $TiSe_2$ mounted on Si_3N_4 shortly after exfoliation and after a month of exposure to air, respectively. The insets are selected area diffraction patterns taken inside the white circles. **(c),(d)** HAADF-STEM images in a smaller area after exfoliation and after a month of exposure. The inset of (c) is a color view of the STEM image. Figure adapted from [22].

the process begins on the surface and slowly spreads inwards.

Chapter 5

The Circular Photogalvanic Effect

The circular photogalvanic effect (CPGE) will serve as the probe for studying the chiral CDW transition in $TiSe_2$. Here, we describe what the CPGE is, highlight an experiment where it was used to measure particle chirality, and describe specifically how it is should be sensitive to chiral ordering in $TiSe_2$.

5.1 Phenomenology

The CPGE is characterized by the emergence of photocurrents in response to circularly polarized (CP) light. It can be phenomenologically described by

$$J_\alpha = \eta_{\alpha\beta\gamma}(\omega)\varepsilon_\beta(\omega)\varepsilon^*_\gamma(\omega) \tag{5.1}$$

where the indices run through the crystal axes $\{a, b, c\}$, J_α is the photocurrent in the α direction, ε is the electric field from the laser light, ω is the light frequency, and $\eta_{\alpha\beta\gamma}$ is a rank-3 tensor called the second-order optical susceptibility [12] [28]. The imaginary part of $\eta_{\alpha\beta\gamma}$ gives rise to the CPGE. Importantly, $\eta_{\alpha\beta\gamma}$ is intrinsic to the system and encodes its symmetries. Thus, the CPGE can be understood by considering broken or absent symmetries regardless of the specific microscopic phenomena at play. For example, $\eta_{\alpha\beta\gamma}$ must vanish if the crystal is centrosymmetric, so no CPGE would be observable. The presence of any mirror symmetry M_i requires

that $\eta_{\alpha\beta\gamma}$ be zero if it contains an odd number of the i index.

The tensor $\eta_{\alpha\beta\gamma}$ can be expressed as

$$\eta_{\alpha\beta\gamma} = \frac{\pi e^3}{\hbar V}\epsilon_{\beta\gamma j}\sum_{n,m} f^{\gamma}_{nm}\Delta^{\alpha}_{\gamma,nm}r^{\gamma}_{\gamma,nm}r^{j}_{\gamma,mn}\delta(\hbar\omega - E_{\gamma,mn}), \tag{5.2}$$

where V is the system volume, $E_{\gamma,mn} = E_{\gamma,m} - E_{\gamma,n}$ is the difference between the band energies, $f^{\gamma}_{nm} = f^{\gamma}_{n} - f^{\gamma}_{m}$ is the difference between the Fermi-Dirac distributions, $r_{\gamma,nm} = i\langle n|\,\partial_{\gamma}\,|m\rangle$ is the Berry connection across the gap, $\Delta^{\alpha}_{\gamma,nm} = \partial_{\gamma_\alpha}E_{\gamma,nm}/\hbar$, and $\hbar$ is the reduced Planck constant [29]. Equation 5.2 captures part of the microscopic picture behind the CPGE, as it explicitly depends on band energies, carrier distributions and the Berry curvature, meaning the CPGE can also provide information about these quantities and not just about broken symmetries.

5.2 CPGE in Weyl Semimetals

The power of the CPGE can be best illustrated by briefly highlighting experiment in which it was used. Ma and Xu *et al.* used the CPGE to measure the chirality of Weyl fermions in tantalum arsenide (TaAs) [12]. In condensed matter systems, Weyl fermions are quasiparticles that act as sources or drains of Berry curvature. Because of their chirality, right/left circularly polarized (RCP/LCP) light can only excite RCP/LCP Weyl fermions. Figure 5-1 shows the photocurrent data for this system along two different crystal axes. In Fig 5-1a, the CPGE is allowed by symmetry, and we see that the photocurrent oscillates as the light polarization switches between RCP and LCP. Figure 5-1b shows the lack of a CPGE along a different crystal axis. TaAs has a mirror symmetry that forbids the CPGE along this direction. The different curves with different offsets in both (a) and (b) arise from the thermal currents excited by shining the laser on different sample spots. Using this data and knowledge of the crystal symmetries, Ma and Xu *et al.* were able to extract the exact contribution from each Weyl fermion and independently determine their chirality.

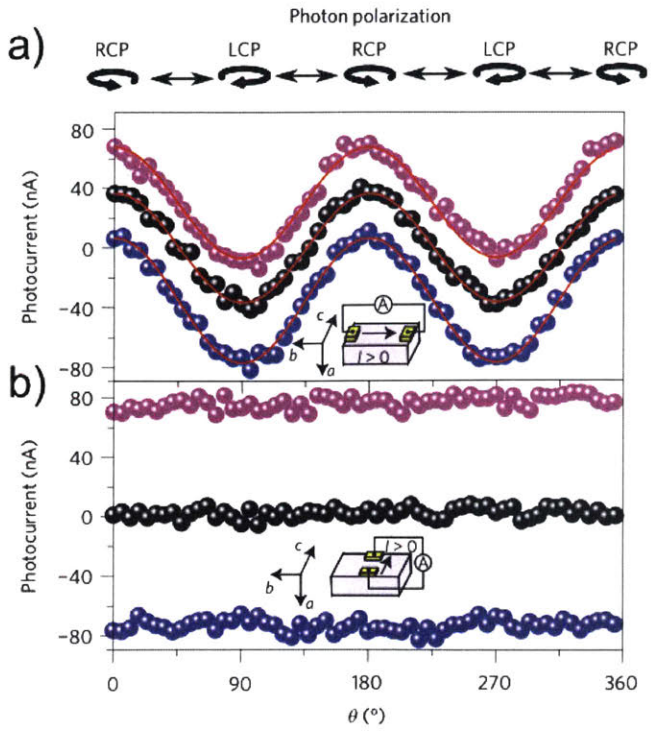

Figure 5-1: The CPGE in the Weyl semimetal TaAs. **(a)** The CPGE along the $-b$ direction, allowed from symmetry considerations. **(b)** No CPGE is observed along the c direction since it is forbidden by symmetry. Figure adapted from [12].

5.3 The CPGE and Chiral Charge Ordering

The CPGE in any direction is forbidden in bulk $TiSe_2$ because the crystal is centrosymmetric, both in its normal and non-chiral CDW phases. However, the chiral phase spontaneously breaks inversion, all mirror and roto-inversion symmetries. Therefore, chiral-ordered $TiSe_2$ should exhibit a polarization-tunable photocurrent along the the out-of-plane c axis. Additionally, the CPGE measurements can be readily performed at different temperatures in a cryostat, so we can determine the chiral transition temperature by looking for the onset of the CPGE as a function of temperature.

The CPGE measurements would conclusively show the existence of the chiral CDW phase and is not hindered by the issues in the experiments performed by Ishioka *et al.* and Castellan *et al.* [7] [9]. An out-of-plane CPGE in the absence of an in-plane response is unique to the chiral CDW order that has been proposed. Furthermore,

laser light can penetrate through the whole sample and excite the bulk electronic states, meaning that the CPGE is a result of chiral order persisting throughout $TiSe_2$ and not a surface effect.

Chapter 6

Device Fabrication

6.1 Bottom Contacts

Because the $TiSe_2$ samples are nanometer-sized and sensitive, it is impossible to directly contact them with wires to measure their electrical properties. Instead, we create bottom contacts on the size scale of the flake, which extend out into large pads that can in turn be bonded with wires. First, the pattern has to be etched on the substrate in order to subsequently evaporate the metal and create the electrodes [30].

6.1.1 Electron Beam Lithography

To etch the desired pattern, first we cover a SiO_2 substrate with a layer of poly(methyl methacrylate) (PMMA), as shown in Figure 6-1a. PMMA is sensitive to high-energy electrons, so a desired pattern is created by selectively shining an electron beam on those areas, as depicted in Figure 6-1b, in a process referred to as electron beam lithography (EBL). The electron beam etches away the irradiated PMMA, and leaves behind the contact outline.

6.1.2 Metal Deposition

Next, the sample is held under high vacuum over a PdAu alloy. The metal is heated with an electron beam until it sublimates and deposits on to the substrate, as illus-

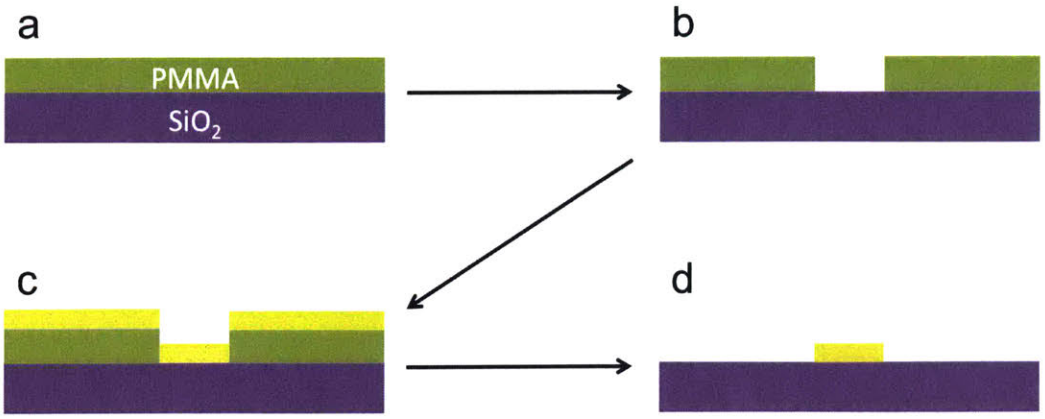

Figure 6-1: **(a)** SiO_2 substrate covered in PMMA. **(b)** A specific region of PMMA is etched away with an electron beam. **(c)** Sublimated PdAu alloy (in yellow) is evaporated on to the surface of the SiO_2 and PMMA. **(d)** The PMMA is dissolved with acetone, leaving behind the metal that was in contact with the substrate.

trated in Figure 6-1c. The process can be carefully controlled to evaporate precise thicknesses.

Once the whole sample is evenly covered with around 20 nm of the alloy, the substrate is submerged in acetone to dissolve and wash away the PMMA. Thus, only the PdAu that was in direct contact with the SiO_2 remains on the chip, as shown in Figure 6-1d, and the contact geometry is successfully attained.

6.2 Exfoliation

Mechanical exfoliation is the process by which sticky tape is used to peel off layers of bulk crystals and generate suitable flakes for experimental studies. Below we describe the procedure and considerations for the three 2D materials needed for our fabrication: $TiSe_2$, graphene and hexagonal boron nitride (hBN).

6.2.1 $TiSe_2$

To obtain suitable $TiSe_2$ flakes, we mechanically exfoliated bulk crystals with sticky tape. Although generally used to obtain ultrathin flakes in the few nanometer thickness range, it readily works for attaining bulk flakes in the 100 nm range, appropriate

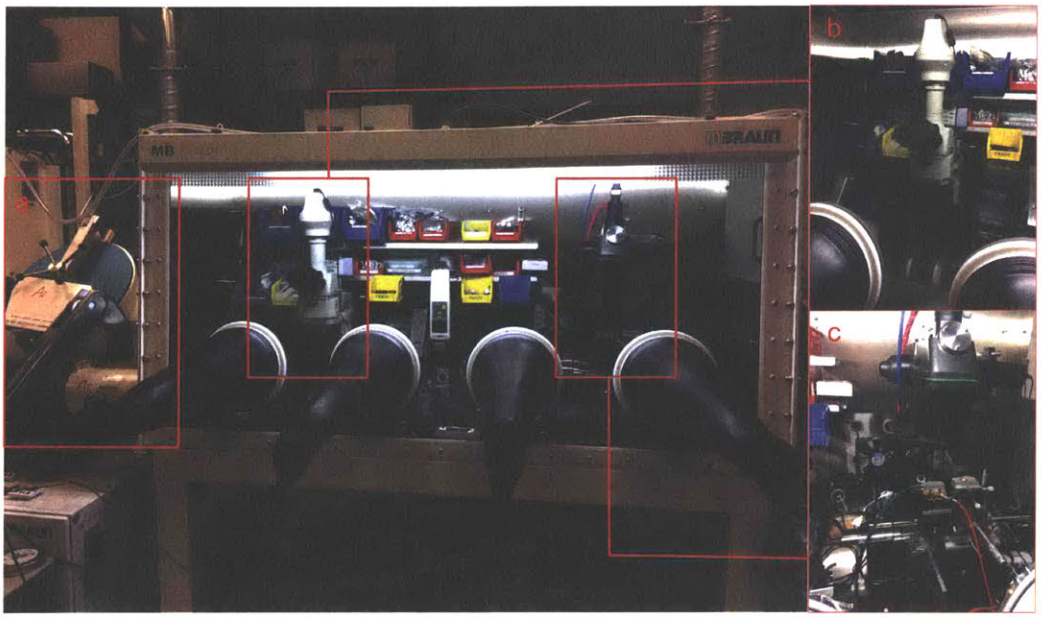

Figure 6-2: Photograph of the Jarillo-Herrero group's glovebox. The atmosphere inside is pure argon, and the H_2O and O_2 levels are kept below 0.1 ppm. **(a)** The vacuum chambers used to take materials in and out of the glovebox. **(b)** The platform and microscope used for exfoliation and flake hunting. **(c)** The transfer set up used for pick ups and transfers. Both the microscope and the transfer set up can be remotely controlled with computers (not shown here).

for this specific experiment. The sticky tape technique is preferred over other exfoliation and growth methods because it typically produces high quality samples with minimal contamination.

As explained in Section 4.5, $TiSe_2$ readily degrades under atmospheric conditions. For this reason, $TiSe_2$ is handled inside a glovebox with an argon atmosphere, shown in Figure 6-2. Pumps and filters keep the O_2 and H_2O levels well below 0.1 ppm, ensuring samples are well protected from degradation. In the event of a leak, the application of a negative pressure gradient will push out the argon and prevent (or slow down in case of serious leaks) the intrusion of air until the issue is resolved (this is also what causes the gloves to stick out).

Figure 6-3 shows the exfoliation process as performed outside the glovebox and with graphene for clarity, although the process is identical when done inside the glovebox and with $TiSe_2$. Figure 6-3a shows the bulk crystal source used for the illustrative exfoliation. We start by placing a small piece of the bulk crystal on a

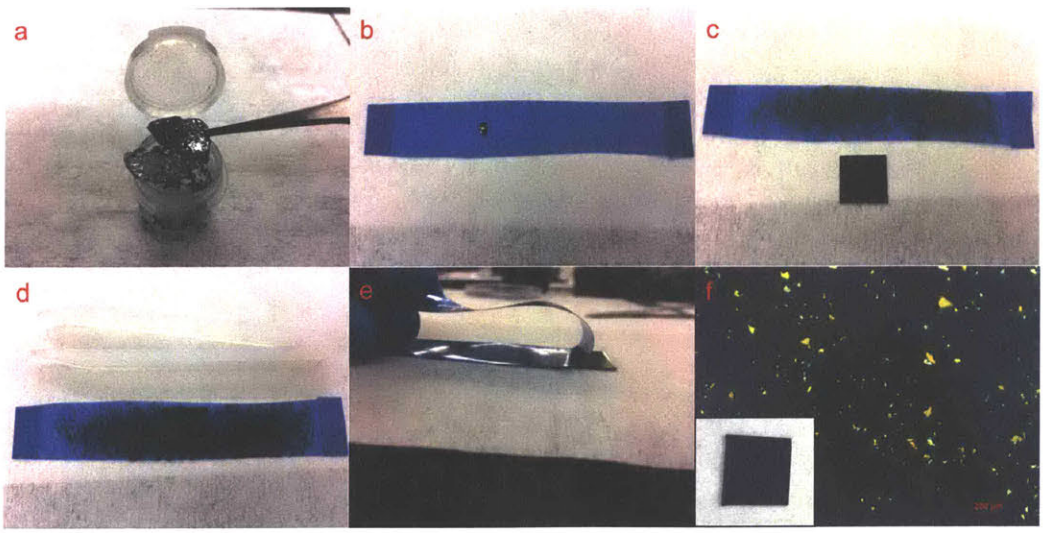

Figure 6-3: A typical exfoliation. **(a)** A bulk graphene crystal used for the exfoliation. **(b)** A small piece of the bulk crystal placed on tape. **(c)** The tape and exfoliated graphene after folding the tape on itself several times; the SiO_2 substrate that will be used is also shown. **(d)** The tape pressed down on the substrate with fingers and teflon tweezers (shown at the top). **(e)** Peeling off the tape in order to deposit the exfoliated flakes on the chip. **(f)** An optical microscope image of the exfoliated chip. The inset shows a camera photo of the exfoliated chip.

piece of tape, as shown in Figure 6-3b. Next, in Figure 6-3c, the tape is folded on itself several times in order to peel off the top layers of the bulk crystal and spread the flakes evenly throughout the surface. Generally, denser exfoliations are better for increasing the yield of desirable flakes. Next, the tape is placed on a silicon chip and pressed on with fingers and teflon tweezers, as in Figure 6-3d. Afterwards, we slowly peel off the tape as depicted Figure 6-3e. During the final step, some of the top layers of the exfoliated source will be deposited on the SiO_2. Figure 6-3f shows the exfoliated chip under a microscope, where flakes of varying thicknesses can be seen. The inset of 6-3f shows the chip, and, looking closely, it is possible to see very thick flakes that were left behind by the tape.

Using an optical microscope, we can scan the surface of the silicon chip and search for suitable flakes. Different thicknesses will interact with light differently, thus exhibiting different colors. Therefore, flake thickness can be reliably determined via optical contrast. In most TMDs, thinner flakes will look somewhat purple, and thicker flakes will appear yellow. Optical contrast is best suited for determining the thick-

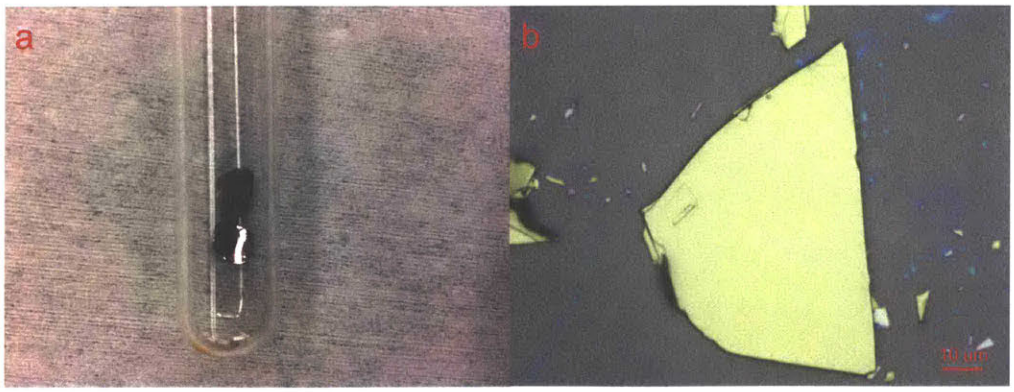

Figure 6-4: **(a)** Bulk $TiSe_2$ source, courtesy of the Gedik group. **(b)** The $TiSe_2$ flake used for Device 3.

ness of few-layer crystals since the change in color is significant in this regime. For thicker ones, it is more difficult to determine the specific number of layers, although this is generally not an issue since bulk properties will not depend sensitively on layer number.

For our experiment, we are interested in bulk flakes around 100 nm thick (light-yellow color, see Fig. 6-4b) because the objective is to measure the out-of-plane current from the bottom to the top of the sample. Furthermore, large-area flakes are preferred over smaller ones so local regions can be probed with the laser. Lastly, we aim for flat surfaces in order to avoid surface defects and to facilitate the other fabrication steps. Figure 6-4 shows the bulk $TiSe_2$ source used for exfoliation, and the flake used for one of the devices.

6.2.2 Graphene and hBN

Next, we need graphene and hBN flakes. Although graphene has many exciting properties and is the subject of much ongoing research, its use here is simple: as the top metal contact. As explained in Section 6.1, we make our bottom contacts by etching a pattern and evaporating PdAu on to the SiO_2 chip. Afterwards, the $TiSe_2$ is transferred on to the substrate (detailed in the Section 6.3). Direct etching and metal deposition on to the sample could damage it. Therefore, it is best to transfer the graphene flake on to the $TiSe_2$ and connect it to the already deposited metal

contacts. Because graphene is an excellent conductor and a layered 2D material, it will both have a clean interface and will make good contact with the sample.

To obtain high quality crystals, graphene is exfoliated as in Secton 6.2.1. However, now few-layer flakes that can cover all or most of the $TiSe_2$ sample's surface area are preferred. Furthermore, graphene is not air-sensitive so it can be handled outside of the glovebox.

In addition to graphene, hBN is used for sample encapsulation. This 2D material is insulating, and a large-area flake with a thickness of around 20 to 30 nm is used to cover the whole sample (or, at least, the area contacted by the graphene) to protect it from the outside environment. This step allows us to take the finished device outside the glovebox and load it into the cryostat without worrying about short-term degradation.

6.3 Transfer

After finding appropriate flakes, they are picked up and transferred on to the pre-made gold contacts. Meanwhile, we have to ensure the process does not damage or contaminate the sample. Luckily, clean and efficient transferring is possible thanks to polycarbonate (PC) slides [31].

6.3.1 PC Slide Fabrication

To fabricate a PC slide, we begin with a clean glass slide and deposit a few drops of a 6% solution of PC on the surface using a pipette. Then, another glass slide is placed on top, which helps the PC to spread evenly along the slide. Once it has spread thoroughly, we quickly slide the top one off, leaving behind an uniform surface of PC that quickly dries and solidifies.

Next, we cut a small square of polydimethsylsiloxane (PDMS), a transparent, flexible organic compound, and place it on another clean glass slide. The PDMS serves as an elevated surface to facilitate the pick up and transfer of flakes.

Afterwards, we puncture a hole just slightly larger than the PDMS into a piece of

tape. We place the tape on the PC-covered glass slide, ensuring the hole is aligned with a smooth and clean area, and gently peel it off along with the PC.

Finally, we align the hole in the tape with the PDMS on the other glass slide, and place it down ensuring a smooth interface between the PDMS and PC to avoid wrinkles. Thanks to the elevated PDMS, there is now a PC "bubble" around it that can be used to pick up and transfer nanoscale flakes.

We find that the PC becomes stiffer as time passes, making them harder to use. Thus, it is best to use slides that are no more than 2 to 4 weeks old. Furthermore, the stiffness and stickiness of the PC is heavily dependent on the atmospheric moisture at the moment of fabrication. Generally, the more moisture in the air, the better the quality. The problem can be ameliorated on drier days by allowing the PC to dry on top of a damp wipe for 10 minutes while covered with a Petri dish.

6.3.2 Transfer Set Up

First, we describe in detail how pick ups and transfers are performed for a general flake, and then we elaborate on the nuances of our specific device. To perform a pick up and/or transfer, the PC slide and exfoliated substrate are mounted on to a transfer set up as shown in Figure 6-5. The apparatus allows for precise control over the position of both components. With a built-in optical microscope, the surfaces of the PC slide and substrate can be visualized, making it possible to carefully align flakes in the case of multi-step pick ups. The substrate stage also has a built in heater to control the temperature during the process.

6.3.3 Pick up

Once the PC slide and target flake are aligned as desired, we lower the PC slide tilted at a 2° to 4° angle until it makes makes initial contact with the substrate. The tilt is necessary to ensure the PC does not suddenly touch at an unexpected spot, as the slight angle guarantees the edge will touch first.

Figure 6-6a-c show a pick up as seen from the microscope in the transfer set up.

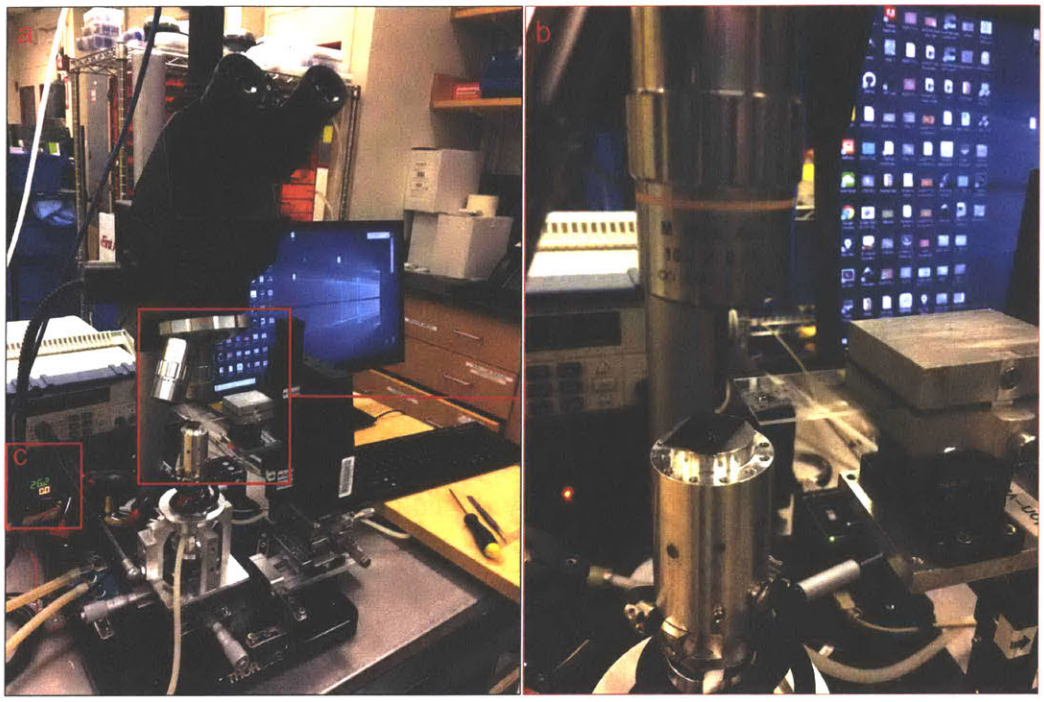

Figure 6-5: **(a)** The Jarillo-Herrero High-Precision Transfer Set Up **(b)** Close up of the microscope, substrate and PC slide. **(c)** The temperature control box.

After the initial contact, we bring the PC wavefront close to the flake by lowering the slide. Once it is close enough, the sample is heated for two purposes. First, the heat will cause the the PC and PDMS to expand and pass over the flake in a more controlled manner than might be otherwise achievable with the mechanical motor. Secondly, the stickiness of the PC increases as a function of temperature, so it is necessary to heat up to between 95°C and 105°C in order for the PC to become adhesive enough to actually pick up the flake. It is possible to go to higher temperatures for more difficult pick ups, but that includes the risk that the PC will stick to the substrate.

We allow the system to heat at the target temperature for around 3 minutes to ensure good contact and thermalization. To disengage, we turn the heat off and let the PC smoothly contract on its own over the desired flake. After it disengages, we use the motor to pull the rest of the PC slide up until it is longer touching the substrate. It is best to disengage between 60°C and 90°C; below that range, the PC becomes too stiff and could either fail to pick up the flake or rip. Ideally, the flake will stick to the PC and the pick up is successful. If it fails, it is possible to try

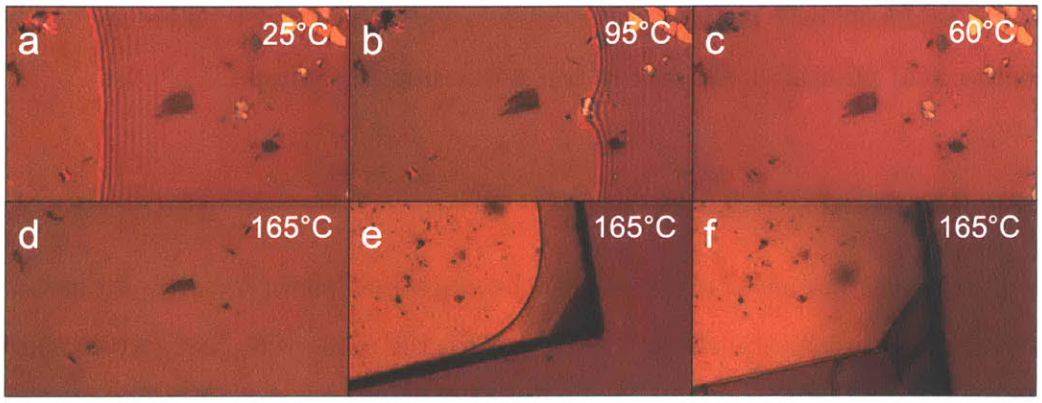

Figure 6-6: A graphene pick up and transfer on to a new subtrate. **(a)** The PC wavefront is brought close to the target graphene flakes in the center. **(b)** The substrate is heated, causing the PC to expand and envelop the graphene. **(c)** The chip is allowed to cool, which causes the PC to retract over the target flakes. Note how the color contrast of the top flake has changed, indicating it was successfully picked up, while the bottom flake was not. **(d)** The PC slide used to pick up the graphene is heated to 165°C on a new substrate. **(e)** After thermalizing, the PC is lifted up until it separates from the PDMS. **(f)** The PC slide is further lifted up until the PC rips from the PDMS and sticks to the substrate, successfully completing the transfer.

again with the same slide but by heating to a higher temperature and/or letting it thermalize for a longer time. If that does not work, a different PC slide should be used. In some cases, degradation will cause the flakes to stick very strongly to the substrate and make them impossible to pick up, so it is best to use freshly-exfoliated flakes whenever possible.

Lastly, only if the transfer set up is precise enough, it is possible to perform the pick up by first heating the substrate to the target temperature and then using the mechanical motor to slowly engage the flake. In our specific case, this latter method seems to work better for pick ups performed in atmospheric conditions, while the heat-engage procedure above works better inside the glove box. Whether this is due to some difference in the transfer set ups or due to the different environmental factors, we do not know.

Multiple pick ups can be performed with the same PC slide to make stacks in cases where different materials are required for the final device. Naturally, the topmost flake in the stack is picked up first, and the bottommost is done last. In fact, this

method is preferred over pick ups and transfers with different PC slides, as it shortens fabrication and minimizes the risk of contaminating the sample.

6.3.4 Transfer

Once all the pick ups are completed and the stack has been prepared, we mount the target substrate on the transfer set up. We align the stack with the bottom contacts, and lower the tilted PC slide until the edge makes contact with the chip. Again, the SiO_2 is heated so the wavefront smoothly engages the stack. However, for a transfer, it is necessary to heat up to at least 160°C in order for the PC to stick well to the substrate. Figure 6-6d-f show a transfer as seen from the microscope in the transfer set up

Once at 160°C, we slowly pull the PC slide up with the mechanical motor until the PC detaches fully from the PDMS. Now, the PC needs to fully rip from the slide and stay on the substrate. To achieve this, we move the slide in the x-y directions, stretching and ripping the PC. Care must be taken because too much pulling will lift the PC off the substrate and carry the stack away with it. If the PC does not rip, the slide can be slightly lowered so that the stretched PC folds on to the heated substrate and becomes easier to tear. Additionally, higher temperatures will make the process easier, but the higher heat can damage sensitive materials. After the sample has cooled back down to room temperature, we submerge it in chloroform for 30 minutes to 2 hours in order to dissolve the PC.

6.3.5 $TiSe_2$, Graphene and hBN

For the fabricated devices, the $TiSe_2$ was picked up and transferred independently, even though it is at the bottom of the stack, because bulk flakes are generally harder to pick up and could crack the thinner flakes that make up the top part of the stack. The PC was dissolved normally.

Next, we made a graphene/hBN heterostructure by first picking up the top hBN and then the graphene. Subsequently, the stack was transferred on to the $TiSe_2$ and

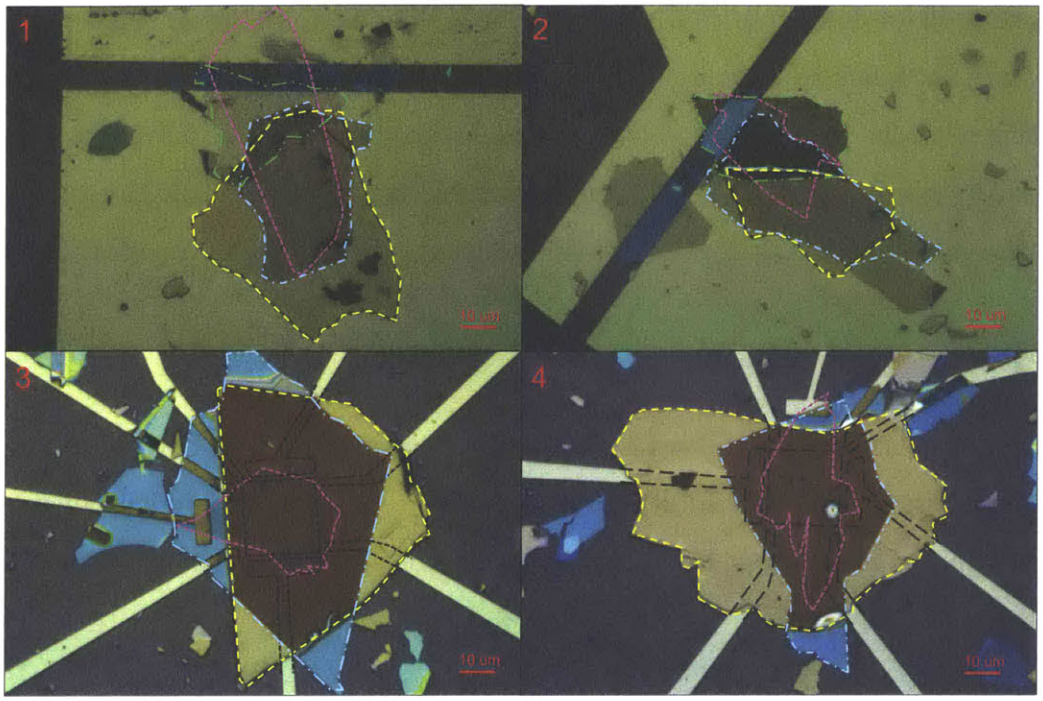

Figure 6-7: The four devices that were fabricated and measured. Yellow: $TiSe_2$, pink: top graphene, blue: top hBN, green: bottom hBN, black: outlines of bottom contacts.

the sample was again submerged in chloroform. Generally, more than one dissolution can pose a problem, but bulk $TiSe_2$ is robust and more resistant to contamination.

6.4 Devices

Below we present the four devices we fabricated and measured. They all consist of a $TiSe_2$/graphene/hBN stack on top of 20 nm PdAu contacts.

6.4.1 Devices 1 and 2

Devices 1 and 2 consist of a large gold pad separated from a gold contact. The $TiSe_2$ flake rests on the large pad near its edge, and is connected to the other contact with graphene. Thus, we can measure the current that flows from the bottom pad, across the sample and out through the graphene (or vice versa), which corresponds to the out-of-plane current.

There are a few flaws with the device geometry. First, the gold pad is unnecessarily

large so it slows down fabrication. Second, it is difficult to perfectly align the $TiSe_2$ flake with the edge, so we must also use a bottom hBN to prevent the graphene from shorting with the bottom pad. Lastly, and most importantly, the device geometry is insensitive to in-plane currents. This is crucial, because a CPGE along the a-b plane is not allowed by symmetry, so we must show that this is the case in the measurements.

6.4.2 Devices 3 and 4

Devices 3 and 4 correct the flaws from the first two samples. The bottom pad is now much smaller, and the the addition of a Hall-bar contact geometry will allow us to measure in-plane currents. Furthermore, no bottom hBN is necessary since there is no danger of shorting.

Chapter 7

Results and Analysis

7.1 Measurement Set Up

Figure 7-1 shows a schematic of the measurement system used. A CO_2 laser with a photon energy of 120 meV reflects off a mirror into a linear polarizer. Next, it reflects off a two-axis scanning mirror into a series of lenses that focus the laser on the sample. Before reaching the $TiSe_2$, the beam goes through a rotatable quarter waveplate. When the quarter waveplate rotates relative to the first polarizer, the light polarization changes from linear, to RCP, to linear, to LCP, back to linear, and so forth. As the laser strikes the sample, it will generate a photocurrent that can flow through the bottom contacts and into an external circuit that can capture the signal. The two-axis scanning mirror can make small adjustments in the position of the beam, providing the capability to scan the beam over the sample and generate a photocurrent "map" such as that shown in Figure 7-2b. Additionally, the sample is mounted inside of a cryostat through which cold helium gas can flow, providing the capability to perform measurements down to 50 K.

7.2 Large Linear Photogalvanic Effect

We present data from Device 1, whose optical image is shown in Figure 7-2a. Figure 7-2b shows a typical CPGE "map" obtained when the laser spot is scanned across

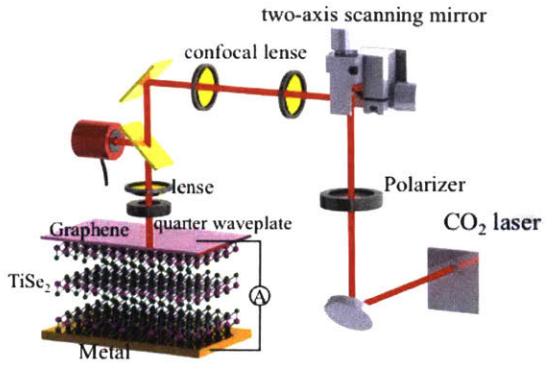

Figure 7-1: A schematic of the experimental set up. A CO_2 laser with an energy of 120 meV goes through a polarizer, shines off of a two-axis scanning mirror and passes through a quarter waveplate before striking the sample. The polarization of the light can vary between linear, RCP and LCP as the quarter waveplate rotates relative to the first polarizer. The two-axis scanning mirror can control the position of the laser spot. Lastly, the bottom contact and top graphene are connected to an external circuit to measure the photocurrent. The device is kept under vacuum and in a cryostat where the temperature can be varied.

the sample and the photocurrent is measured as a function of position. Observe how there is a nonzero response only where the graphene contacts the $TiSe_2$ since that is the only area where current can be measured. The photocurrent response along the dashed black line is shown in Figure 7-2c,d at 250 K and 150 K, respectively. At 250 K, there is a periodic modulation with maxima corresponding to linear polarized (LP) light, evident in the line-cut data points from the dashed line. The response is due to the the linear photogalvanic effect (LPGE), the LP analog of the CPGE.

At 150 K, below the expected chiral transition temperature, the LPGE is still present, and there is no CPGE. However, the lack of a response to CP light can be explained by the two-fold degeneracy of the chiral ground state [10]. In the absence of an external excitation, the CW and CCW states have the same energy, so at T_{chiral}, where the system is forced to pick a certain orientation, it will presumably choose one or the other with equal probability. Therefore, it is natural to assume that there will be an equal number of LCP and RCP domains, whose photocurrent response would cancel each other out and generate a net zero CPGE. Furthermore, although the presence of the LPGE is unexpected, its emergence both below T_{chiral} and above

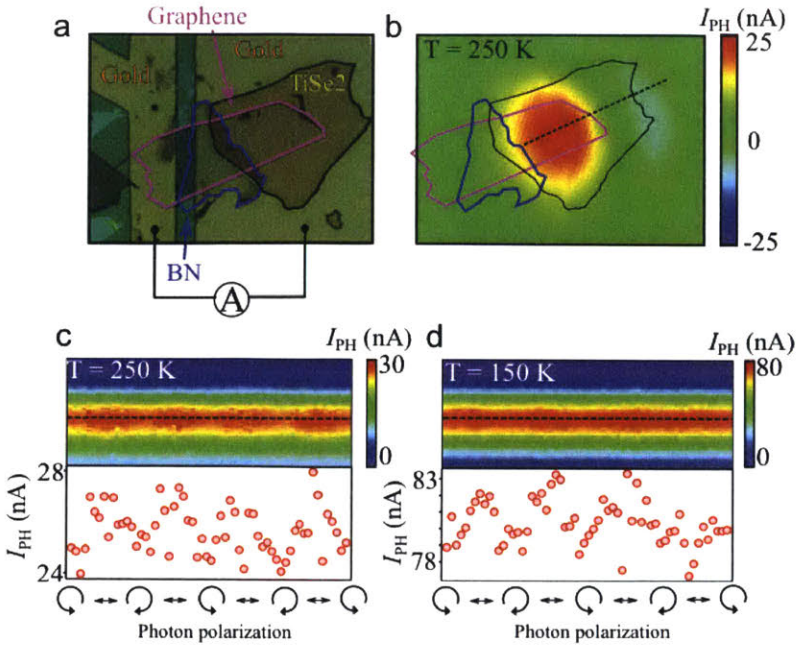

Figure 7-2: Photocurrent response of $TiSe_2$. **(a)** Optical image of the measured device with outlines provided for the top graphene and bottom hBN flakes. **(b)** A photocurrent "map" showing the response intensity when the laser shines on a specific position of the sample. There is only a nonzero response where it would be measurable: the contact between the $TiSe_2$ and graphene. **(c,d)** Top: photocurrent along the dashed line in (b) as a function of polarization at 250 K and 150 K, respectively. Bottom: Line cut from the dashed line in the top frame.

T_{CDW} suggests that the underlying mechanism is unrelated to charge or chiral order. Nevertheless, to properly understand the nature of the chiral CDW phase, we must find a way to both suppress the LPGE and to amplify the CPGE.

7.3 Chiral Training

It is possible to favor the formation of the CW or CCW chiral phases by breaking the ground state degeneracy. This can be achieved by cooling the sample past T_{chiral} while exposed to light of the corresponding chirality, effectively training the system. Figure 7-3 shows the training data for both LCP and RCP light. After cooling down the sample to 50 K, the photocurrent is measured as a function of photon polarization. After training with LCP (Fig. 7-3a-c) or RCP (Fig. 7-3e-g), the system shows

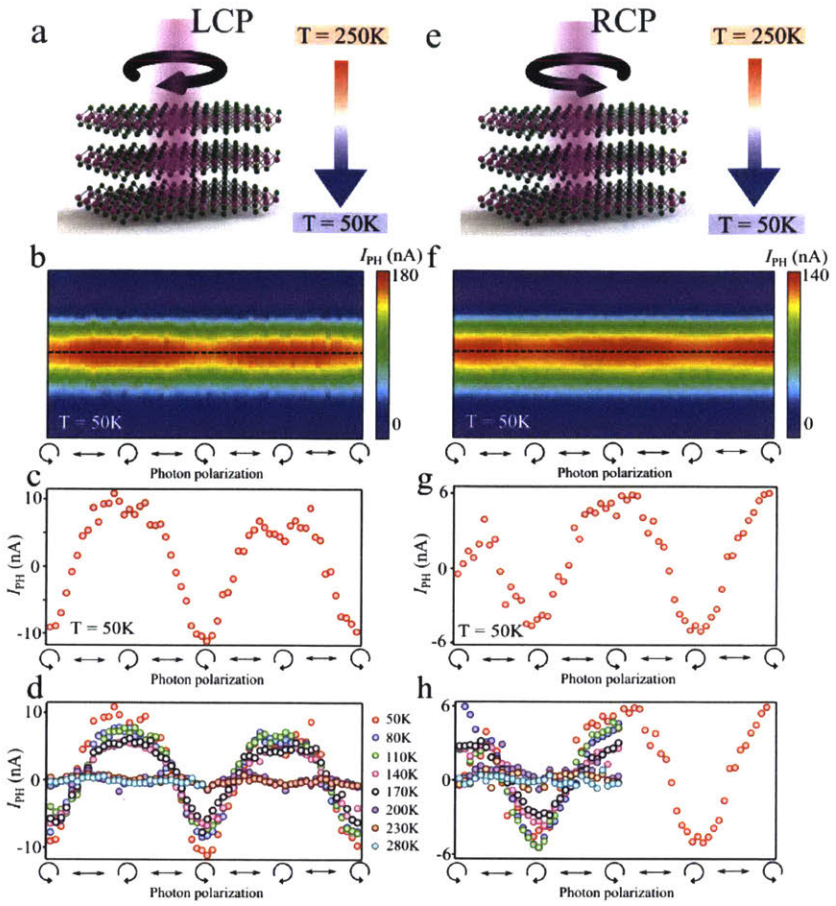

Figure 7-3: Chiral training of $TiSe_2$. **(a)** The system is cooled from 250 K to 50 K while shining LCP light on it. **(b)** Photocurrent intensity as a function of position (vertical axis) and polarization (horizontal axis). **(c)** Photocurrent line cut along the dashed line from (b). The CPGE is clearly observable. **(d)** Temperature dependence of the CPGE as the sample is warmed after training.**(e)-(h)** Same as (a)-(d) but with RCP training.

a CPGE response with maximum signal at the polarization with which it was trained and no perceivable LPGE. This indicates that when the sample was cooled under the influence of a chiral beam it preferentially selected the chiral-ordered state corresponding to the photon polarization. Further, the observation of the CPGE means that the material remains in the trained configuration even after the polarization is varied at a lower temperature, as opposed to changing its handedness.

Figure 7-3d,h shows the temperature dependence of the CPGE as the sample is cooled under LCP and RCP light, respectively. Above 200 K, there is no CPGE. Below 170 K, the CPGE is fully turned on and its amplitude does not seem to

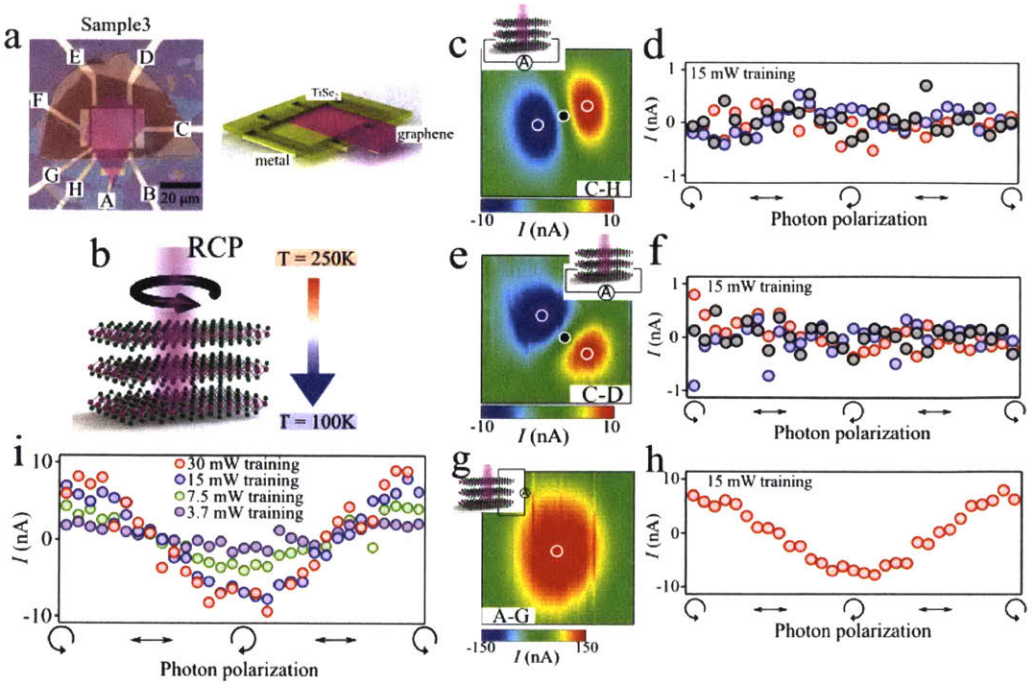

Figure 7-4: In-plane and out-of-plane photocurrents in Device 3. **(a)** Optical image of Device 3 with overlayed flake images for clarity. The electrodes are labeled A through H. **(b)** All data is taken after the system has been trained with RCP photons from 250 K down to 100 K. **(c)** In-plane photocurrent measured across C-H. **(d)** Polarization dependence of the photocurrent at the blue, red and black points in (c). **(e),(f)** Same as (c), (d) but measuring the photocurrent across C-D. **(g)** Global out-of-plane photoresponse of the sample. **(h)** CPGE at the white-outlined circle in (g) **(i)** Power dependence of the CPGE.

depend sensitively on temperature. The transition temperature, therefore, must lie somewhere between 170 K and 200 K, in agreement with the 183 K observed by Castellan *et al.* [9]. Note, also, how the CPGE is not sensitive to the regular CDW transition, as expected, which should occur around 205 K.

All the data shown up to this point has come from Device 1. As explained in the previous chapter, Devices 1 and 2 have the major flaw that they cannot detect in-plane currents. So, although the system exhibits and out-of-plane response, the possibility of an in-plane CPGE cannot be ruled out yet, which would violate the chiral state symmetries. We now present data from Device 3, which can measure in-plane responses thanks to the Hall bar geometry of the bottom contacts.

Figure 7-4a presents an optical image of Device 3. The electrodes are labeled with a capital letter A through H. The sample is trained with RCP photons and cooled to 100 K. Figure 7-4c shows the current map generated when the laser is scanned across the sample and the signal from the in-plane C-H probes is measured. The signal is zero almost everywhere except for a local (blue) minimum and a (red) maximum. Figure 7-4d shows the polarization dependence of the current at the two extrema and in between them (black). There is no in-plane CPGE on any of the three areas, as expected from symmetry considerations. The results are reinforced by similar data taken between probes C-D, shown in Figure 7-4e,f. The spatial variation of the current is due to thermally excited carriers from laser heating, and does not intrinsically arise from a photoresponse.

The out-of-plane CPGE is still present, shown in Figure 7-4g,h, as previously observed in Device 1. The power dependence of the CPGE, after training, is shown in Figure 7-4i. The maximum photocurrent increases with power, and an almost null response at 3.7 mW suggests that is the minimum power needed to activate the system. Further, the chiral domains could not be flipped by, for example, first training with RCP photons, switching to LCP (or vice versa), and increasing the power. If this occurred, then no CPGE would be observed, but a photocurrent modulation was present up until the maximum power of 120 mW that the CO_2 laser can output. Thus, the domain wall at low temperatures is stiff, although in principle it should be possible to flip its chirality if a high enough power is used.

7.4 Chiral Transition

Theoretical models and previous experiments suggest that the transition into a chiral state occurs below T_{CDW} [9] [10]. Therefore, the onset of the CPGE should begin below the previously observed $T_{CDW} = 205$ K, while the data from Figure 7-3 indicates it should occur above 170 K.

The CPGE is not sensitive to the regular CDW transition, so instead we rely on resistivity measurements to identify it. Figure 7-5a shows the resistivity versus

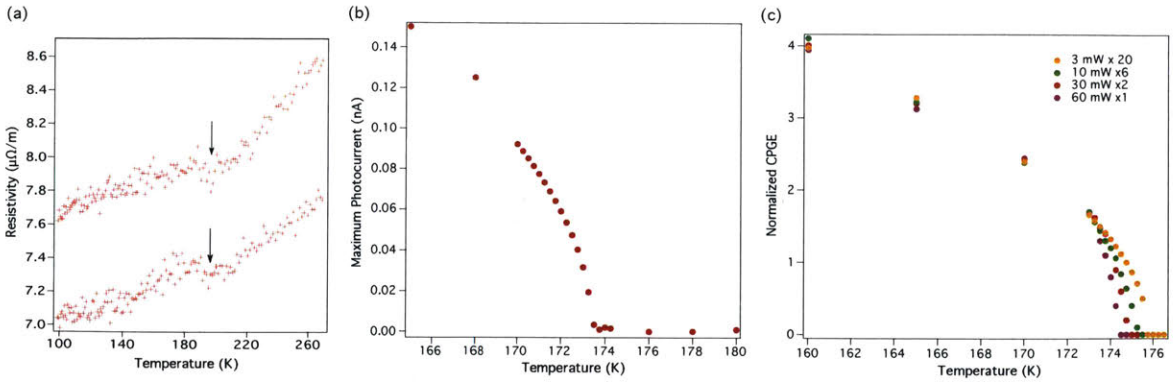

Figure 7-5: CDW and chiral transitions. **(a)** Temperature dependence of the resistivity in Devices 4, where the CDW transition is observed around 197 K. **(b)** Temperature dependence of the maximum CPGE in Device 3 as the sample is warmed up after being trained with 30 mW RCP light. **(c)** Normalized maximum CPGE as a function of temperature showing the power variation of the chiral phase transition.

temperature for Device 4. The sample exhibits a kink around 197 K, confirming the CDW phase transition. It is slightly lower than the accepted value of 205 K, likely owing to stoichiometric variations in the crystal growth or defects introduced during fabrication.

Next, the sample is trained with RCP light down to 100 K and the maximum photocurrent is measured as the sample is warmed up. The results are shown in Figure 7-5b. As the temperature increases, the current decreases, indicating a weakening of the CPGE. At around 174 K, the signal completely vanishes and the system has transitioned into a non-chiral CDW state. Thus, we find that $T_{chiral} \simeq 174$ K, below T_{CDW} in agreement with previous experiments and theoretical predictions.

Figure 7-5c shows the normalized power dependence of the chiral transition. The sample is trained with RCP light at 30 mW, and warmed up with different powers. T_{chiral} depends slightly on the applied power; it is around 174 K for 60 mW and almost 176 K for 3 mW.

7.5 Discussion

As presented in Chapter 5, the expression for the CPGE is

$$J_\alpha = \eta_{\alpha\beta\gamma}(\omega)\varepsilon_\beta(\omega)\varepsilon^*_\gamma(\omega) \tag{7.1}$$

where the indices run over the crystallographic directions. $TiSe_2$ only exhibits exhibits an out-of-plane J_c while $J_{a,b}$ are both zero. The specific result can only be explained by a lack of inversion, all mirror, and roto-inversion symmetries, a scenario unique to chiral ordering. Therefore, the observed CPGE has to arise because the system attains a chirality, and not due to some other mechanism.

Furthermore, we were able to train the chirality of the phase by cooling down under the influence of CP light. After training, the samples showed different CPGE behavior, dependent on the polarization, analogous to trained magnetic systems in external magnetic fields. However, tight-binding models predict that the photocurrent should not depend on the system chirality but only on the electron density, which is the same regardless of the training. Nevertheless, chiral molecules exhibit chirality-dependent electron transfer under the influence of CP light [32]. To understand the phenomenon, consider a transport model where electrons tunnel across a potential bridge from a donor site to an acceptor site. CP light will excite electrons in adjacent sites with the same amplitude but different complex phase. Thus, as the electrons travel across the bridge, they interfere with each other and lead to different final acceptor amplitudes. Therefore, the photocurrent in $TiSe_2$ will depend on both the chirality of the phase and on the handedness of the excitation. Given that both phases are opposite, the CPGE should be reversed, as observed.

The fact that the chirality cannot be flipped at low temperatures suggests that the domain wall is soft only near T_{chiral}. This is further supported by the observed variation of T_{chiral} with laser power. Thus, flipping the domain chirality should be possible within the temperature range of 174 K to 176 K, making it possible, at least in principle, to observe a hysteresis loop within that range. However, those measurements are technically challenging and were not undertaken in this study. To

perform them, the sample would have to be trained with a certain power to low T, and subsequently kept at 174-176 K while varying the polarization and power. The experiment is left for the future.

The observation of a phase transition into chiral state is remarkable because chirality is typically an intrinsic property. This means that $TiSe_2$ spontaneously breaks all mirror, inversion, and roto-inversion symmetries at T_{chiral}, and enters a gyrotropic state. Spontaneous gyrotropic ordering has also been suggested in cuprates [33] [34] [35]. This further suggests that $TiSe_2$ breaks time-reversal symmetry, and could be further probed by looking for Kerr and Faraday rotations, an effect that occurs when the linear polarization of incident light is slightly rotated upon reflection or transmission, respectively.

We have observed gyrotropic ordering in $TiSe_2$, but the underlying mechanism remains to be elucidated. One possible model is put forth by van Wezel (see Section 4.3), where the system undergoes simultaneous charge and orbital ordering, and so the CDW vectors are rotated relative to each other in successive layers in order to minimize the free energy. A second explanation could be that $TiSe_2$ becomes an excitonic insulator (EI) [36] [37]. In an EI, excitons form due to thermal fluctuations across a small band gap. If their binding energy is larger than the gap, then the system is unstable and the excitons will condense into a coherent ground state. The condensate will arrange itself along any of the three inequivalent directions in the Brillouin zone, and so it is possible that the interlayer Coulomb interaction will cause them to order in a chiral manner. Finally, another mechanism could be a combination of spin-orbit coupling and strong electron-electron interactions [38]. In such a system, the CDW along each inequivalent direction will have a different spin polarization due to the spin-orbit interaction, so chiral order could emerge as a combination of interlayer Coulomb and spin effects.

Lastly, the origin of the observed LPGE remains unknown. It could arise from the photon drag effect [39]. The phenomenon occurs when LP light transfers momentum to excited carriers. Therefore, even in a symmetric band, there will be a net photocurrent arising from asymmetric momentum transfer. There could also be an

induced asymmetry owing to the interface of the $TiSe_2$ with the graphene and PdAu contacts. Nevertheless, why it emerges in untrained $TiSe_2$ below and above T_{CDW}, and why it vanishes after training with CP light, remain open questions.

Chapter 8

Conclusion

We have fabricated $TiSe_2$/graphene/hBN devices in order to study the chiral CDW phase in 1T-$TiSe_2$. The symmetry breaking-sensitive CPGE was used to probe a suggested chiral transition in the material, as chiral ordering implies that inversion, all mirror, and roto-inversion symmetries are broken. Indeed, $TiSe_2$ exhibits spontaneous gyrotropic ordering at $T_{chiral} \simeq 174K$, below the well-studied normal CDW transition around ~200 K. Furthermore, the material was successfully trained using chiral light into a system with like-handedness. No in-plane CPGE was observed below T_{chiral}, guaranteeing the uniqueness of the out-of-plane photoresponse as originating from chiral order along the crystal c-axis. The study is significant because it posits $TiSe_2$ as one of the first systems that spontaneously attains chirality, a typically intrinsic property. It opens up the door for studying a novel phase in order to elucidate how electrons interact to form nontrivial phases of matter.

However, our study still leaves some unanswered questions. First, the mechanism behind the chiral phase transition remains poorly understood. It can be further elucidated by studying the system with a variety of techniques in order to search for other signatures, like Kerr and Faraday rotations. Secondly, it would be interesting to see whether the system exhibits hysteresis, in other words, if the domain walls can be flipped after they have been trained. Lastly, the mysterious origin of the LPGE and its strange behavior poses a further problem that needs to be addressed.

Future directions remain to be explored with regards to the chiral phase. This

study focused solely on bulk $TiSe_2$, whereas the effects of reduced dimensionality are yet to be explored. Does the chiral phase exist in the ultrathin limit? How does the chiral phase transition depend on thickness? Additionally, superconductivity has been observed in $TiSe_2$ under pressure and when intercalated with copper [40] [41]. How a chiral structure interacts and competes with the formation of Cooper pairs is an interesting question. Lastly, other TMDS such as TaS_2 have a charge ordered phase at low temperatures, so similar systems can also be studied to understand whether the formation of chiral CDWs is more prevalent in 2D systems.

Bibliography

[1] S. Manzeli, D. Ovchinnikov, D. Pasquier, O. V. Yazyev, and A. Kis, "2D transition metal dichalcogenides," *Nature Reviews Materials*, vol. 2, p. 17033, June 2017.

[2] Q. H. Wang, K. Kalantar-Zadeh, A. Kis, J. N. Coleman, and M. S. Strano, "Electronics and optoelectronics of two-dimensional transition metal dichalcogenides," *Nature Nanotechnology*, vol. 7, p. 699, Nov. 2012.

[3] G. Grüner, "The dynamics of charge-density waves," *Rev. Mod. Phys.*, vol. 60, pp. 1129–1181, Oct. 1988.

[4] R. E. Thorne, "Charge-density-wave conductors," *Physics Today*, vol. 49, p. 42, May 1996.

[5] P. Chen, Y. H. Chan, X. Y. Fang, Y. Zhang, M. Y. Chou, S. K. Mo, Z. Hussain, A. V. Fedorov, and T. C. Chiang, "Charge density wave transition in single-layer titanium diselenide," *Nature Communications*, vol. 6, p. 8943, Nov. 2015.

[6] P. Chen, Y.-H. Chan, M.-H. Wong, X.-Y. Fang, M. Y. Chou, S.-K. Mo, Z. Hussain, A.-V. Fedorov, and T.-C. Chiang, "Dimensional effects on the charge density waves in ultrathin films of $TiSe_2$," *Nano Letters*, vol. 16, no. 10, pp. 6331–6336, 2016. PMID: 27648493.

[7] J. Ishioka, Y. H. Liu, K. Shimatake, T. Kurosawa, K. Ichimura, Y. Toda, M. Oda, and S. Tanda, "Chiral Charge-Density Waves," *Physical Review Letters*, vol. 105, p. 176401, Oct. 2010.

[8] B. Hildebrand, T. Jaouen, M.-L. Mottas, G. Monney, C. Barreteau, E. Giannini, D. R. Bowler, and P. Aebi, "Local Real-Space View of the Achiral 1T-$TiSe_2$ Charge Density Wave," *Phys. Rev. Lett.*, vol. 120, p. 136404, Mar. 2018.

[9] J.-P. Castellan, S. Rosenkranz, R. Osborn, Q. Li, K. E. Gray, X. Luo, U. Welp, G. Karapetrov, J. P. C. Ruff, and J. van Wezel, "Chiral phase transition in charge ordered 1T-$TiSe_2$," *Phys. Rev. Lett.*, vol. 110, p. 196404, May 2013.

[10] J. van Wezel, "The chiral charge density wave transition in 1T-$TiSe_2$," *Journal of Physics: Conference Series*, vol. 391, no. 1, p. 012167, 2012.

[11] L. Sun, C. Chen, Q. Zhang, C. Sohrt, T. Zhao, G. Xu, J. Wang, D. Wang, K. Rossnagel, L. Gu, C. Tao, and L. Jiao, "Suppression of charge density wave state in two-dimensional 1T-$TiSe_2$ by atmospheric oxidation," *Angewandte Chemie (International ed. in English)*, vol. 56, June 2017.

[12] Q. Ma, S.-Y. Xu, C.-K. Chan, C.-L. Zhang, G. Chang, Y. Lin, W. Xie, T. Palacios, H. Lin, S. Jia, P. A. Lee, P. Jarillo-Herrero, and N. Gedik, "Direct optical detection of Weyl fermion chirality in a topological semimetal," *Nature Physics*, vol. 13, pp. 842–847, Sept. 2017.

[13] K. S. Novoselov, A. K. Geim, S. V. Morozov, D. Jiang, Y. Zhang, S. V. Dubonos, I. V. Grigorieva, and A. A. Firsov, "Electric Field Effect in Atomically Thin Carbon Films," *Science*, vol. 306, pp. 666–669, Oct. 2004.

[14] K. S. Novoselov, D. Jiang, F. Schedin, T. J. Booth, V. V. Khotkevich, S. V. Morozov, and A. K. Geim, "Two-dimensional atomic crystals," *Proceedings of the National Academy of Science*, vol. 102, pp. 10451–10453, July 2005.

[15] A. Kuc, N. Zibouche, and T. Heine, "Influence of quantum confinement on the electronic structure of the transition metal sulfide TS_2," *Phys. Rev. B*, vol. 83, p. 245213, June 2011.

[16] K. F. Mak, C. Lee, J. Hone, J. Shan, and T. F. Heinz, "Atomically thin MoS_2: A new direct-gap semiconductor," *Phys. Rev. Lett.*, vol. 105, p. 136805, Sept. 2010.

[17] X. Xi, Z. Wang, W. Zhao, J.-H. Park, K. T. Law, H. Berger, L. Forró, J. Shan, and K. F. Mak, "Ising pairing in superconducting $NbSe_2$ atomic layers," *Nature Physics*, vol. 12, p. 139, Nov. 2015.

[18] E. Navarro-Moratalla, J. O. Island, S. Mañas-Valero, E. Pinilla-Cienfuegos, A. Castellanos-Gomez, J. Quereda, G. Rubio-Bollinger, L. Chirolli, J. A. Silva-Guillén, N. Agraït, G. A. Steele, F. Guinea, H. S. J. van der Zant, and E. Coronado, "Enhanced superconductivity in atomically thin TaS_2," *Nature Communications*, vol. 7, p. 11043, Mar. 2016.

[19] Y. Yang, S. Fang, V. Fatemi, J. Ruhman, E. Navarro-Moratalla, K. Watanabe, T. Taniguchi, E. Kaxiras, and P. Jarillo-Herrero, "Enhanced Superconductivity and Suppression of Charge-density Wave Order in 2H-TaS_2 in the Two-dimensional Limit," *ArXiv e-prints*, Oct. 2017.

[20] V. Fatemi, S. Wu, Y. Cao, Q. Gibson, Q. Gibson, K. Watanabe, T. Taniguchi, R. Cava, and P. Jarillo-Herrero, "Gate-Accesible Superconductivity and Helical Modes in Monolayer WTe_2," *APS Presentation*, Mar 2018.

[21] Y. Lin, *Optical Properties of Two-Dimensional Transition Metal Dichalcogenides.* PhD thesis, Massachusetts Institute of Technology, 2014.

[22] J. P. Eisenstein and A. H. MacDonald, "Bose–Einstein condensation of excitons in bilayer electron systems," *Nature*, vol. 432, p. 691, Mar. 2004.

[23] P. Rivera, J. R. Schaibley, A. M. Jones, J. S. Ross, S. Wu, G. Aivazian, P. Klement, K. Seyler, G. Clark, N. J. Ghimire, J. Yan, D. G. Mandrus, W. Yao, and X. Xu, "Observation of long-lived interlayer excitons in monolayer $MoSe_2$–WSe_2 heterostructures," *Nature Communications*, vol. 6, p. 6242, Feb. 2015.

[24] R. Peierls, "Zur Theorie der elektrischen und thermischen Leitfähigkeit von Metallen," *Annalen der Physik*, vol. 396, no. 2, pp. 121–148, 1929.

[25] K. Rossnagel, L. Kipp, and M. Skibowski, "Charge-density-wave phase transition in $1T - TiSe_2$: Excitonic insulator versus band-type Jahn-Teller mechanism," *Phys. Rev. B*, vol. 65, p. 235101, May 2002.

[26] J. van Wezel, P. Nahai-Williamson, and S. S. Saxena, "Exciton-phonon-driven charge density wave in $TiSe_2$," *Phys. Rev. B*, vol. 81, p. 165109, Apr. 2010.

[27] K. Rossnagel, "On the origin of charge-density waves in select layered transition-metal dichalcogenides," *Journal of Physics: Condensed Matter*, vol. 23, no. 21, p. 213001, 2011.

[28] L. Wu, S. Patankar, T. Morimoto, N. L. Nair, E. Thewalt, A. Little, J. G. Analytis, J. E. Moore, and J. Orenstein, "Giant anisotropic nonlinear optical response in transition metal monopnictide Weyl semimetals," *Nature Physics*, vol. 13, p. 350, Dec. 2016.

[29] F. de Juan, A. G. Grushin, T. Morimoto, and J. E. Moore, "Quantized circular photogalvanic effect in Weyl semimetals," *Nature Communications*, vol. 8, p. 15995, July 2017.

[30] N. Nair, *Photon-Induced Tunneling in Graphene-Boron Nitride-Graphene Heterostructures.* B.S. Thesis, Massachusetts Institute of Technology, 2013.

[31] P. J. Zomer, M. H. D. Guimarães, J. C. Brant, N. Tombros, and B. J. van Wees, "Fast pick up technique for high quality heterostructures of bilayer graphene and hexagonal boron nitride," *Applied Physics Letters*, vol. 105, p. 013101, July 2014.

[32] R. J. Cave, "Inducing chirality with circularly polarized light," *Science*, vol. 323, no. 5920, pp. 1435–1436, 2009.

[33] J. Xia, E. Schemm, G. Deutscher, S. A. Kivelson, D. A. Bonn, W. N. Hardy, R. Liang, W. Siemons, G. Koster, M. M. Fejer, and A. Kapitulnik, "Polar Kerr-Effect Measurements of the High-Temperature $YBa_2Cu_3O_{6+x}$ Superconductor: Evidence for Broken Symmetry near the Pseudogap Temperature," *Physical Review Letters*, vol. 100, p. 127002, Mar. 2008.

[34] P. Hosur, A. Kapitulnik, S. A. Kivelson, J. Orenstein, and S. Raghu, "Kerr effect as evidence of gyrotropic order in the cuprates," *Physics Review B*, vol. 87, p. 115116, Mar. 2013.

[35] P. Hosur, A. Kapitulnik, S. A. Kivelson, J. Orenstein, S. Raghu, W. Cho, and A. Fried, "Erratum: Kerr effect as evidence of gyrotropic order in the cuprates [Phys. Rev. B 87, 115116 (2013)]," *Physics Review B*, vol. 91, p. 039908, Jan. 2015.

[36] H. Cercellier, C. Monney, F. Clerc, C. Battaglia, L. Despont, M. G. Garnier, H. Beck, P. Aebi, L. Patthey, H. Berger, and L. Forró, "Evidence for an excitonic insulator phase in 1T-$TiSe_2$," *Phys. Rev. Lett.*, vol. 99, p. 146403, Oct. 2007.

[37] B. Zenker, H. Fehske, and H. Beck, "Fate of the excitonic insulator in the presence of phonons," *Phys. Rev. B*, vol. 90, p. 195118, Nov 2014.

[38] L. Fu, "Parity-Breaking Phases of Spin-Orbit-Coupled Metals with Gyrotropic, Ferroelectric, and Multipolar Orders," *Physical Review Letters*, vol. 115, p. 026401, July 2015.

[39] J. W. McIver, D. Hsieh, H. Steinberg, P. Jarillo-Herrero, and N. Gedik, "Control over topological insulator photocurrents with light polarization," *Nature Nanotechnology*, vol. 7, pp. 96–100, Feb. 2012.

[40] A. F. Kusmartseva, B. Sipos, H. Berger, L. Forró, and E. Tutiš, "Pressure induced superconductivity in pristine 1T-$TiSe_2$," *Phys. Rev. Lett.*, vol. 103, p. 236401, Nov. 2009.

[41] E. Morosan, H. W. Zandbergen, B. S. Dennis, J. W. G. Bos, Y. Onose, T. Klimczuk, A. P. Ramirez, N. P. Ong, and R. J. Cava, "Superconductivity in Cu_xTiSe_2," *Nature Physics*, vol. 2, p. 544, July 2006.